Investigation of Air-Bridge-Waveguide Photonic Bandgap Structures

by

Constantine Nikolaos Tziligakis

Submitted to the Department of
Electrical Engineering and Computer Science
in partial fulfillment of the requirements for the degree of

Master of Science
in Electrical Engineering and Computer Science

at the

MASSACHUSETTS INSTITUTE OF TECHNOLOGY

September 1996

Author .....
.....
Department of
Electrical Engineering and Computer Science
August 9, 1996

Certified by .....
.....
Erich P. Ippen
Elihu Thomson Professor of Electrical Engineering
Thesis Supervisor

Accepted by .....
.....
ic R. Morgenthaler
Chairman, Departmental Committee on Graduate Students

Αφιερωνεται στους γονεις μου

Νικολαο και Γεωργια

και τον αδελφο μου

Ιωαννη.

Investigation of Air-Bridge-Waveguide Photonic Bandgap Structures

by

Constantine Nikolaos Tziligakis

Submitted to the Department of
Electrical Engineering and Computer Science
on August 9, 1996, in partial fulfillment of the
requirements for the degree of
Master of Science
in Electrical Engineering and Computer Science

Abstract

A new type of microresonator, the photonic bandgap air-bridge, is designed and fabricated. Two tapered and bent waveguides are designed to facilitate coupling light into and out from the structures. A wavelength tunable femtosecond setup is developed to perform experiment on the devices. It is based on a femtosecond Ti:sapphire laser that synchronously pumps an Optical Parametric Oscillator (OPO). The signal and idler pulses from the OPO are then combined in a nonlinear crystal to produce a train of tunable (3.5-5.2 microns) femtosecond pulses at the difference frequency. A coupling stage employing near diffraction-limited optics and high-precision micropositioning equipment as well as a spectrometer and a very sensitive InSb detector are used for performing measurements on the devices.

Thesis Supervisor: Erich P. Ippen
Title: Elihu Thomson Professor of Electrical Engineering

Acknowledgements

I am grateful to Professor Erich Ippen for all his support and guidance during these years. I really enjoyed working with him. His smile, good mood as well as penetrating questions are greatly appreciated.

I am thankful to Professors Leslie Kolodziejski and John Joannopoulos for the nice collaboration we have had over the past two years. Interacting with them as well as their groups has been a really useful experience for me.

Special thanks go to Dr. Stefano Longhi and Siegfried Fleischer. In the few months he has been here, Stefano has helped a lot with his experience and suggestions on this project. His generous help in the lab and useful discussions are gratefully acknowledged. Siegfried has provided a lot of important advice on this experiment. Through these years I benefited a lot from him. I admire his practical way of thinking.

Many thanks to Ed Lim for the nice job he did fabricating these devices. It has been enjoyable to collaborate and learn a lot of fabrication issues from him. I thank Dr. Jerry Chen for running simulations for the bridges and guiding me through his BPM code. His contribution in the design of the structures has been substantial. Shanhui Fan and Dr. Pierre Villeneuve are the people who really made me understand the subtle issues behind the air-bridge resonators and their design.

James Foresi has been helpful in more than one ways. I thank him for making the arrangements for using the lead-salt diode at the Spectroscopy Laboratory, for working together in my first steps with the 5 micron light and for providing useful information and help on coupling issues. I thank all the people in the Spectroscopy lab (Room 6A100) and especially Jon O'Brien, Ilia Dubinsky, Kevin Cunningham and Steven Drucker for their hospitality.

I am thankful to Dr. Gunter Steinmeyer and Erik Thoen for lending me a lot of useful equipment for my experiment. I especially appreciate Gunter's advice and suggestions on this experiment. I

also thank Dr. Shu Namiki for lending me the 980nm diode and Dave Dougherty for his useful advice and his humor. Sharing an office with William Wong, Andrew Ugarov and Jahu-Pekka Laine has really been enjoyable. Thanks to all the rest for providing a pleasant and friendly environment. Special thanks to the secretaries Donna Gale, Cindy Kopf and Mary Aldridge for their help with numerous burocratic issues. I appreciate Cindy's help with the preparation of my poster last year.

This work is dedicated to my parents Nikolaos and Georgia and my brother Ioannis to whom I am grateful for their support and patience during these years.

Contents

1. Photonic Bandgap Materials **9**

1.1 General 9

1.2 The photonic bandgap air-bridge structure 12

2. Design of Photonic Bandgap Air-Bridge Devices for the near IR **18**

2.1 Air-Bridge resonator design 18

2.2 Design of the coupling waveguides 22

2.3 Fabrication 32

3. The experimental setup **35**

3.1 General 35

3.2 The Optical Parametric Oscillator 37

3.3 The Difference Frequency Generation stage 41

4. The coupling stage **47**

4.1 The coupling setup 47

4.2 Coupling light into the structures 51

4.3 The Detectors and the Spectrometer 55

5. Conclusions and Future Work **60**

References **62**

List of Figures

1-1. A photonic bandgap air-bridge resonator.

1-2. Dispersion relation for modes with even symmetry with respect to the xy-plane in the channel waveguide shown in the inset. Only the lowest three bands are shown (form Ref. [15]).

1-3. Vector plot of the electric field associated with the first (a) and the second (b) bands (from Ref. [15]).

1-4. Vector plot of the electric field for the defect mode (from Ref. [15]).

1-5. Normalized transmission through the cavity as a function of frequency (from Ref. [15]).

1-6. Quality factor as a function of the number of holes on either side of the defect (from Ref. [15]).

2-1. Wavelength response of the C1 bridge resonators.

2-2. Schematic overview of the structure with the waveguides.

2-3. Coupling geometry when the output facet is cut (a) and not cut (b).

2-4. The coupling and collimating objectives geometry.

2-5a. The eigenmode at the input of the waveguide when there is no overlayer. The window dimensions are 20x10 microns.

2-5b. The eigenmode at the input of the waveguide with a 0.2 micron overlayer. The window dimensions are 20x10 microns.

2-5c. The eigenmode at the input of the waveguide with a 0.8 micron overlayer. The window dimensions are 5x10 microns.

2-6. Waveguide eigenmode at various positions for the final structure. The window dimensions are 20x5 microns for the upper two figures and 5x4 microns for the lower two figures.

2-7. SEM photograph of the air-bridge resonator. The defect, three holes on either side and the overlayer (etched away at the bridges) can be clearly seen (Courtesy of Kuo-Yi Lim, Prof.

Kolodziejski's group).

3-1. Schematic overview of the experimental setup.

3-2. An Optical Parametric Oscillator cavity.

3-3. Schematic overview of the Ti:sapphire-pumped SPPO. P_1-P_5 are pump mirrors, M_1-M_7 are cavity mirrors, and PR_1-PR_2 are intracavity Brewster prisms. M_{6P}-M_{7P} are cavity mirrors used when the intracavity prisms are inserted. PZT is a piezoelectric transducer (from Ref. [19]).

3-4. Typical output powers from the Ti:sapphire pumped OPO as a function of the wavelength (from Ref. [19]).

3-5. The difference frequency generation setup.

3-6. Type-I phase-matching angle for $LiIO_3$ as a function of the difference wavelength.

3-7. Walk-offs between the various pulses inside $LiIO_3$ as a function of the difference wavelength.

4-1. Experimental setup for coupling light into the air-bridges.

4-2. The construction of a reflective microscope objective.

4-3. Profile of the focused infrared (4.8μm) spot in the horizontal direction. A 18μm Gaussian profile is also shown for comparison.

4-4. Profile of the focused infrared (4.8μm) spot in the vertical direction. A 15μm Gaussian profile is also shown for comparison.

4-5. Spectrum of the lead-salt diode at the threshold current (one scan).

Chapter 1

Photonic Bandgap Materials

In this chapter the motivation and concept of photonic bandgap materials is presented. We focus on a qualitative rather than quantitative description and give some examples where these new materials could find applications. In more detail, the theory behind a new type of resonator, the photonic bandgap air-bridge, is explained. The experimental testing of these structures is the topic of this project.

1.1 General

Photonic Bandgap materials (photonic crystals) are a new class of artificial media with many promising applications in the optical and microwave technology. They were first proposed in 1987 [1], [2] and the basic idea is that one could design materials that affect the properties of photons in much the same way as ordinary solids affect the properties of electrons.

At the microscopic level, the wave nature of electrons gives rise to allowed and forbidden energy bands for their propagation in solids. Conductivity is produced by constructive interference at various scattering directions. At particular energy levels destructive interference from the periodic array of atoms occurs preventing the electrons from propagating. Impurity atoms act as defects and cause localized states to appear inside the stopbands. Crystal disorder hinders electric conductivity and is also responsible for electronic localization at some energies.

The new field of photonic bandgap materials has primarily emerged from the question whether photon localization can be achieved in a similar way as for electrons in semiconductors [3], [4]. Although high Q optical cavities and especially microcavities with their numerous applications in laser physics and quantum electrodynamics can be said to localize light, localization is not complete. For example in Fabry-Perot resonators it occurs in one dimension only and light (in particular spontaneous emission) can escape the cavity. In photonic bandgap materials, one creates a periodically modulated dielectric structure with periodicity of the order of the wavelength of light. Acting as classical waves, photons can then experience coherent scattering and interference and show a behavior that qualitatively resembles that of the electrons in solids. The concept becomes more clear just by comparing the Schroedinger and Maxwell equations for the case of electrons in solids and photons in dielectric media, respectively [5]:

$$\left(\frac{h^2}{2m^*} \cdot \nabla^2 + V(\bar{r}) \right) \psi(\bar{r}) = E\psi(\bar{r}) \qquad (1.1)$$

and

$$\left(\nabla \times \frac{1}{\varepsilon(\bar{r})} \nabla \times \right) \bar{H}(\bar{r}) = \omega^2 \bar{H}(\bar{r}) \qquad (1.2)$$

m^* is the electron's effective mass, V the potential in the solid, ψ the electron wavefunction, ε the dielectric constant and H the magnetic field.

Equations (1.1) and (1.2) are linear eigenvalue problems, whose solutions depend on the potential and dielectric function. Therefore, if one were to construct a material consisting of a periodic array of macroscopic dielectric 'atoms', this would cause a band structure to appear for photons exactly as it happens in the case of electrons. One could also open photonic bandgaps, that is certain ranges of frequencies and directions inside the photonic crystal that electromagnetic waves would not propagate. Photonic crystals with different lattice structures (for example square, triangular, hexagonal, diamond structure) might be made. Theoretical calculations confirm the expectations under the important requirement that the dielectrics used are lossless in the bandgap frequency range [5]. It turns out that a big refractive index difference between the dielectrics used is necessary to make the appearance of a large bandgap possible. An important difference between the electron and photon cases comes from the vectorial nature of Maxwell equations. In

the case of photonic crystals light polarized in different directions will behave differently. To open a complete bandgap one has to ensure that light does not propagate regardless of what its polarization is. An atlas with bandgaps for both cases in many different lattice structures is provided in reference [5]. Another important property of photonic crystals is scalability. By scaling the dimensions of the periodic dielectric structure one is able to move the bandgap range to whatever frequency is desired. In fact, the first experimental studies on photonic crystals have been performed at the microwave frequencies where their fabrication was much easier.

After a bandgap has been opened, a step further is to introduce a 'defect' mode for the electromagnetic field which lies inside the photonic bandgap. This is achieved by breaking the periodicity of the crystal thus destroying the perfect translational symmetry. The nature of the mode at the defect is then evanescent and this means that a localized photonic state , in other words, an ideal optical microcavity has been created. The basic difference between a Fabry-Perot microcavity and the above case is that in the former the mode is actually a scattering resonance, whereas in the latter there is a true bound state with a quality factor limited only by material absorption [6].

The potential of photonic bandgap materials for applications in the optical and microwave technology is impressive. Being perfect reflectors at very wide ranges of frequencies, photonic crystals can be used to control propagation of electromagnetic radiation very efficiently. They can be used for example to dramatically improve the directivity of antennas [7-8], make polarizers [5], create waveguides that guide light tightly [5], [9], or make waveguide bends with radii of curvature less than a wavelength [5], [9]. Introducing defects in the crystals, one can create very high-Q electromagnetic cavities with modal volumes of less than half the wavelength. This suggests a lot of applications to the design of novel types of filters, couplers and low-loss laser microcavities. In a three-dimensional photonic crystal with a defect zero-point fluctuations and losses due to spontaneous emision can be completely suppressed. This is very promising for the development of new single mode, thresholdless laser diodes [1], [10].

One dimensional photonic crystals have been well known for a long time (dielectric mirrors and DFB lasers are two examples). An important step in the field was the discovery of structures that exhibit a complete three-dimensional bandgap [11], [12]. The structure proposed by Ho et. al. [11] has a diamond lattice structure and a complete 3D bandgap appears for refractive index differences larger than 2. Yablonovitch et. al. later proposed and fabricated another structure at microwave length scales [12]. This is a 'three-cylinder' structure with the symmetry of the diamond. It

was actually the first experimental demonstration of a full 3D photonic bandgap (at microwave frequencies). The real challenge for making structures at the much shorter and more important, from the optics point of view, near infrared (IR) wavelengths lies in fabrication. The reason is that fabrication at these wavelengths requires submicron resolution, which makes it more difficult if one is to construct a periodic material in more than one dimensions. Many efforts are currently being made by several groups in the field to realize photonic crystals with various lattice structures at infrared wavelengths [13]. A three-dimensional photonic crystal more suitable for submicron fabrication has been recently proposed [14] and is currently being fabricated at MIT by Prof. Kolodziejski's group.

Another very interesting application idea in the near IR was the proposal of a new type of microcavity, called photonic bandgap air-bridge [15]. It consists of a channel waveguide and a one-dimensional photonic crystal with a defect in the middle. The entire structure is suspended in air to ensure the highest possible refractive index contrast between the waveguide and the surrounding medium (GaAs/air or Si/air). The design and experimental testing of these devices for the infrared wavelength range of 4-5 microns are the goals of this project. A brief theory of the structures is presented in the next paragraph.

1.2 The Photonic Bandgap Air-Bridge structure

The photonic bandgap air-bridge is a new type of microcavity that uses index guiding and a one-dimensional photonic crystal to confine light in three dimensions. It is made of high-index channel waveguides in which a strong periodic variation of the refractive index is added along the axial direction. The periodicity is introduced by etching a series of holes vertically through the waveguide. The entire structure is suspended in air (Figure 1-1). A cavity is formed in the middle by breaking the periodicity at that point. Because of the high index contrast between air and the material used for the waveguide (GaAs or Si with refractive indices of 3.37 and 3.48 respectively at 1.55 microns) the mode inside the cavity is tightly confined. The basic difference with a one-dimensional Fabry-Perot resonator lies in the fact that the air-bridge has both a coplanar geometry and strong field confinement.

In order to find the resonator modes one needs to numerically solve an eigenvalue problem for

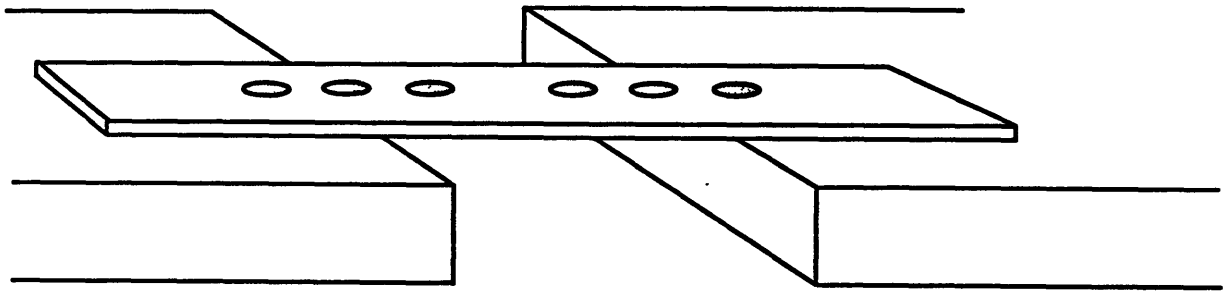

Figure 1-1. A photonic bandgap air-bridge resonator

Maxwell's equations [15], [16]. First, the modes in the waveguide are considered. The dispersion relation for a channel waveguide with a periodic array of holes is shown in Figure 1-2. The width of the structure is taken to be 1.2a, the thickness 0.4a and the diameter of the holes 0.6a, where 'a' is the spacing between the holes. These values have been chosen so as to achieve good field confinement in the cavity. Looking at the graph one clearly sees the gap that is opened between the first and second guided modes of the waveguide. This bandgap extends from f equal to 0.282c/a to f equal to 0.371c/a and is due to destructive interference of light as it is scattered by the holes. In the case of Figure 1-2, the size of the gap is 27% of the midgap frequency. Figure 1-3 shows the electric field for the first two waveguide eigenmodes. In the first one, the field resides mostly in the high index material, whereas in the second it is in the air. There is obviously a large difference in the effective mode index between the two, which explains the bandgap. Introducing a defect with a size corresponding to a quarter-wave phase shift, that is 1.5a, a resonator mode appears inside the bandgap. The larger the defect size, the lower in frequency this resonance mode lies. Figure 1-4 shows a plot of the electric field of the defect mode. It is highly confined in the area around the defect and it decays rapidly along the waveguide. It also has a nodal point at the center. The transverse confinement is very good also (see Figure 2-6). The modal volume is smaller than half a cubic wavelength. Furthermore, the electric field is mostly polarized in the horizontal plane

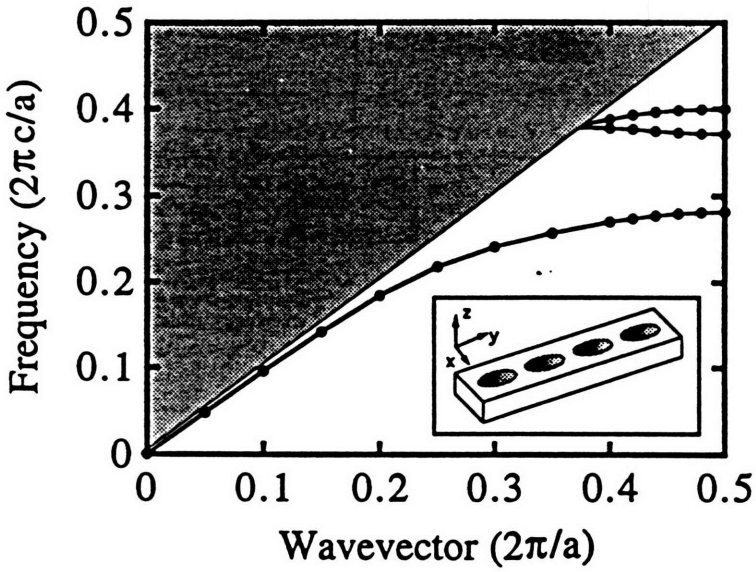

Figure 1-2. Dispersion relation for modes with even symmetry with respect to the xy-plane in the channel waveguide shown in the inset. Only the lowest three bands are shown (from Ref. [15]).

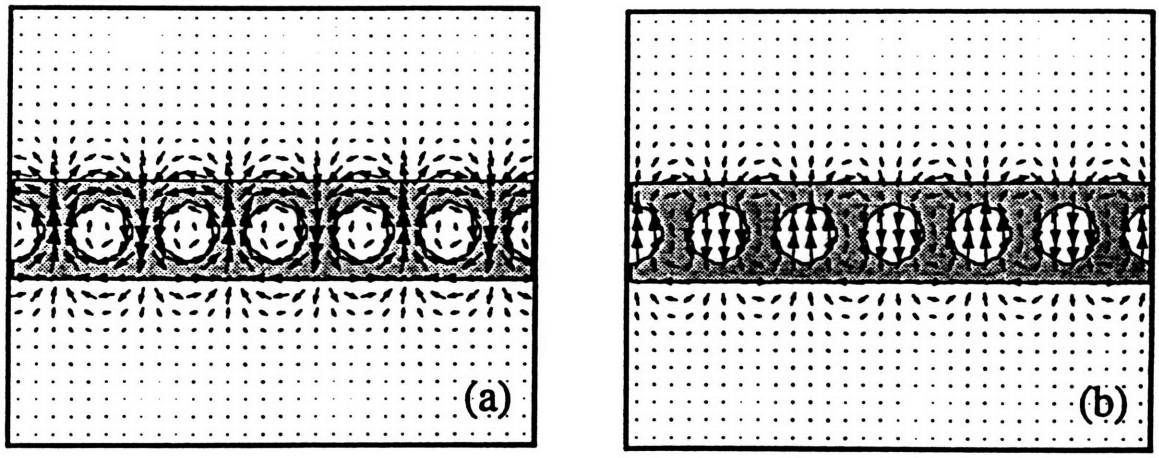

Figure 1-3. Vector plot of the electric field associated with the first (a) and the second (b) bands (from Ref. [15]).

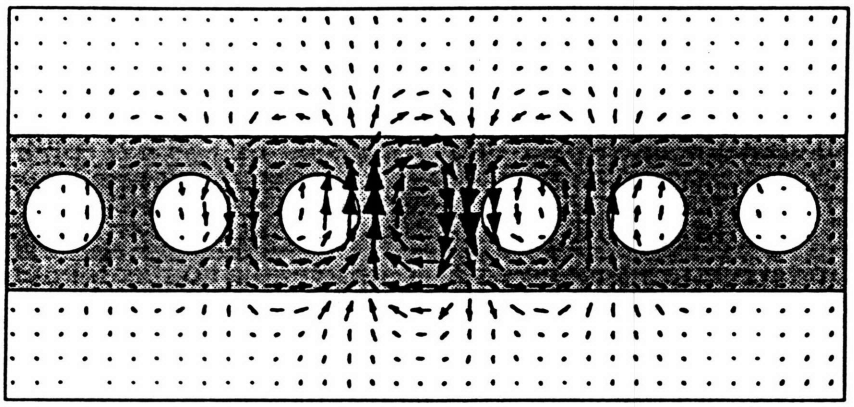

Figure 1-4. Vector plot of the electric field for the defect mode (from Ref. [15]).

and the magnetic field in the vertical (TE-like mode). So, in order to couple light from the waveguide into the defect state, the waveguide mode has to have the same polarization. Figure 1-5 displays the normalized transmission through the cavity versus frequency. For a defect size of 1.5a the resonant mode appears at f=0.313c/a. It is useful to note here, that by increasing the defect size one might bring several states from the upper bands inside the bandgap. The resonator design has to be made carefully to avoid making the cavity multimode. For the case examined here, the separation between the first and second order resonator mode is pretty large (>19% of the midgap frequency) which will allow these waveguides to be operated single-mode.

A very important parameter characterizing the cavity is its quality factor Q. For the air-bridge resonator Q is determined by how well the cavity keeps the mode from leaking into the air that surrounds it and into the channel waveguide. One can define Q_{wg} and Q_{rad} to account for losses due to coupling of the resonator mode to the waveguide and to the radiation modes in the air, respectively. Then, $1/Q = 1/Q_{wg} + 1/Q_{rad}$. Radiation losses are very low in the entire frequency range of the bandgap and do not change much as one increases the number of holes on either side of the cavity. On the other hand, Q_{wg} increases as one adds more holes in the structure. The field is then more confined, but coupling of light from the waveguide into the resonator is reduced.

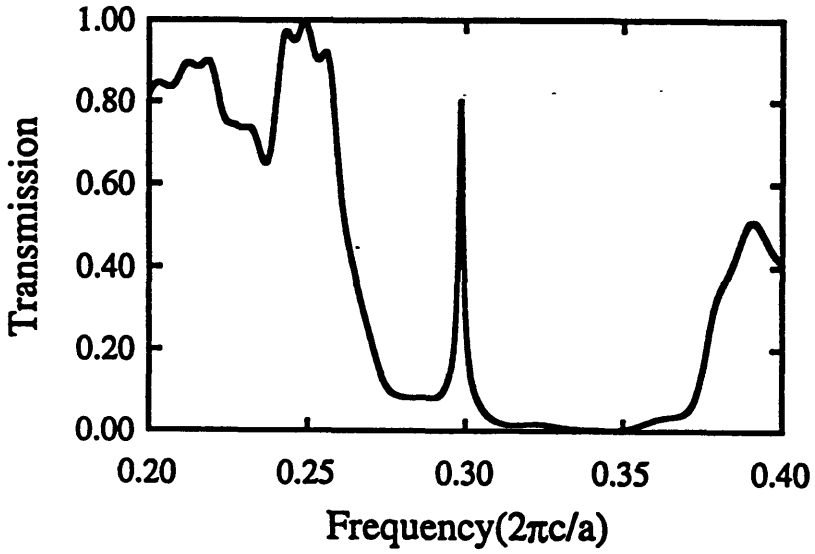

Figure 1-5. Normalized transmission through the cavity as a function of frequency (from Ref. [15])

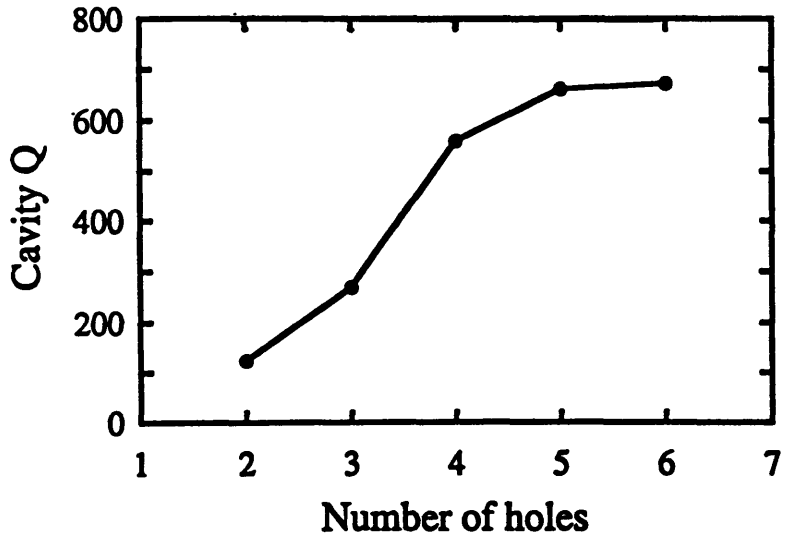

Figure 1-6. Quality factor as a function of the number of holes on either side of the defect (from Ref. [15]).

This is a very important consideration if one is to do experiment with these structures. Basically, when one has a few holes, losses to the waveguides are the dominant factor and Q almost equals Q_{wg} which is small. Increasing the number of holes Q_{wg} becomes larger and larger and after some point radiation losses are the determining factor. Q then saturates around Q_{rad} . This is shown in Figure 1-6, where Q saturates at a value of approximately 700. Really, one cannot increase the Q of the cavity by merely adding more and more holes since the resonant mode is coupled to the continuum. For practical purposes, a compromise has to be reached so that Q is high, but coupling of light from the waveguide into the resonator (and the opposite) is also facilitated. According to Figure 1-6 it seems that a number of 3 or 4 holes on either side with a Q of 270 or 550 is a good choice.

The feasibility of fabricating suspended microstructures with common materials has already been demonstrated by K.Y. Lim and G. Petrich in Prof. Kolodziejski's group [15]. Both the GaAs/AlAs and Si/SiO_2 material groups have been used.

Chapter 2

Design of Photonic Bandgap Air-Bridge Devices for the near IR

In this chapter, we present the issues involved in the design of the air-bridge resonators. In the first part we deal with the resonator itself, and in the second part with the waveguides needed to guide the laser light into the bridges. In the third part, we briefly outline the fabrication procedure and we present some pictures of the devices.

2.1 Air-Bridge resonator design

The air-bridge structure has to provide strong mode confinement and a large bandgap at the wavelengths of interest. Furthermore, it has to have reasonable requirements for its fabrication. In our case it was agreed that optical beam lithography was going to be used for the fabrication of the devices. Optical beam lithography is less challenging than electron beam or X-ray lithography, which is very important when one tries to fabricate a device for the first time. In fact, the first demonstration of suspended microstructures was done by the MIT fabrication team using optical beam lithography [15]. By using optical beam lithography, however, one is not able to realize the small features that are possible with the other two techniques. As a result, the structures are designed for the wavelength range of 4 to 5 microns instead of the more appealing 1.55 micron

wavelength, the standard for the optical communications technology of today.

Some important considerations have to be taken into account in the design of an air-bridge resonator. First, the material used has to have high refractive index. Along with the air that surrounds the bridge, this provides the strong index guiding required for mode confinement in the transverse directions. In our case GaAs and $Ga_xAl_{1-x}As$ alloys are used (GaAs for the bridge). The refractive index of $Ga_xAl_{1-x}As$ varies from 2.85 (x=0) to 3.3 (x=1) at the wavelength of 4.5 microns. Second, one has to ensure strong periodic variations for the refractive index along the bridge waveguide in order to have a large bandgap and to realize a strong resonator mode confinement. In our case, this is achieved by etching a series of air holes along the axial direction of the bridge. Third, it is very important that the designed resonator be single mode. If the cavity were multimode there would be serious losses from radiation into the air since there would be a strong mismatch between the higher cavity modes and the waveguide eigenmode. The singlemodedness of the resonator depends on the defect size (see Chapter 1). For the air-bridge structure a defect size of 1.5a, where a is the spacing between the air-holes, represents a quarter-wave shift and ensures a single TE-like mode in the cavity. Fourth, one has to make a decision on the number of holes that are going to be etched on either side. Their number affects both the Q of the resonator and the ability to couple light into the structure efficiently. As explained in Chapter 1, the more holes one has, the larger the Q is but also the smaller the coupling efficiency from the waveguide into the resonator becomes. In our case, we go for three holes on either side.

In fact, the design of the bridge is more complicated than it seems at a first glance. Parameters as the holes' size and spacing, bridge width and thickness and defect size affect the properties of the air-bridge in interdependent and not so straightforward way. For example, the hole spacing determines more or less the center wavelength of the resonator mode and the defect size; but, in conjunction with the size and the number of holes, it also affects the Q of the cavity. Making the holes larger increases Q and decreases our ability to couple into the structure. In determining the hole diameter one has to take into account also the bridge width which affects the position of the bandgap and the value of Q. The bandgap and resonator mode position and confinement depend also on the bridge thickness. Note that by changing parameters like the hole size and the bridge width and thickness one essentially alters the effective index of the structure which is the basic reason why the bandgap and the resonator mode center wavelength move. In Chapter 1 we presented values for the parameters that lead to an optimized (as much as possible) performance of the struc-

tures. In terms of the hole spacing 'a', which is determined by the resonator mode center frequency f_c from $0.313c/f_c$, these are given by : defect size = 1.5a, hole diameter = 0.6a, bridge width = 1.2a and bridge thickness = 0.4a. The bandgap extends from $f_1 = 0.282c/a$ to $f_2 = 0.371c/a$.

Fabrication imposes some limitations by itself. The optical beam lithography setup at MIT is limited to a 0.4 to 0.5 micron minimum resolvable feature. If one aims at a λ_c of 4.4 microns, then according to the numbers given above 'a' has to be ~1.38μm. The bridge width will be 1.65μm and the hole diameter 0.82μm. One clearly sees that the distance between the edges of two neighboring holes is 0.56μm and that between the hole edge and the bridge edge is ~0.4μm. These two features, especially the second one, are very close to the fabrication limits. A compromise has to be reached. This task was undertaken by Shanhui Fan and Dr. Pierre Villeneuve in Prof. Joannopoulos' group and Ed Lim and Dr. Gale Petrich in Prof. Kolodziejski's group. They decided to make the bridge wider and place the holes further apart. They also made the holes a bit larger. Since making the hole-bridge edge distance and the hole spacing larger has an effect of "adding" dielectric material to the structure and pushing the mode up in wavelength, care has to be taken to somehow "subtract" material from the bridge. This was accomplished by making the bridge thinner and ensures that the resonator center wavelength stays unaltered after the whole procedure. An immediate effect of this redesign is evident on the Q of the cavity. Making the hole spacing larger, the bridge thinner and still keeping the same number of holes, reduces the Q of the resonator significantly. Table 1 presents the three different bridge structures C1, C2 and C3 that are fabricated on the sample along with the resonance center wavelength and the cavity Q of each one of them. Observe the important reduction in the cavity Q when compared to the value of ~270 that one had with the three-hole optimized structure in Chapter 1 (Figure 1-6). Also note that the hole-to-bridge edge distance is still very close to 0.4μm, which represents a challenge for the fabrication. In Figure 2-1 we show the expected wavelength response of the C1 bridge resonators as calculated by Shanhui Fan and Pierre Villeneuve. For a center wavelength of ~4.55μm, the bandgap extends from ~3.9μm to ~5.1μm and the power transmission through the resonator is ~60% (the graph displays amplitude transmission).

Table 1: Fabricated bridge structures (dimensions in μm)

Type	C1	C2	C3
# of holes	3	3	3
a	1.6	1.8	2.0
defect	2.3	2.5	2.7
hole dia.	0.8	1.0	1.2
width	1.6	1.8	2.0
thickness	0.4	0.4	0.4
total length	12.5	13.5	14.9
λ_c	4.55	4.95	>5.10
Q	46	43	-

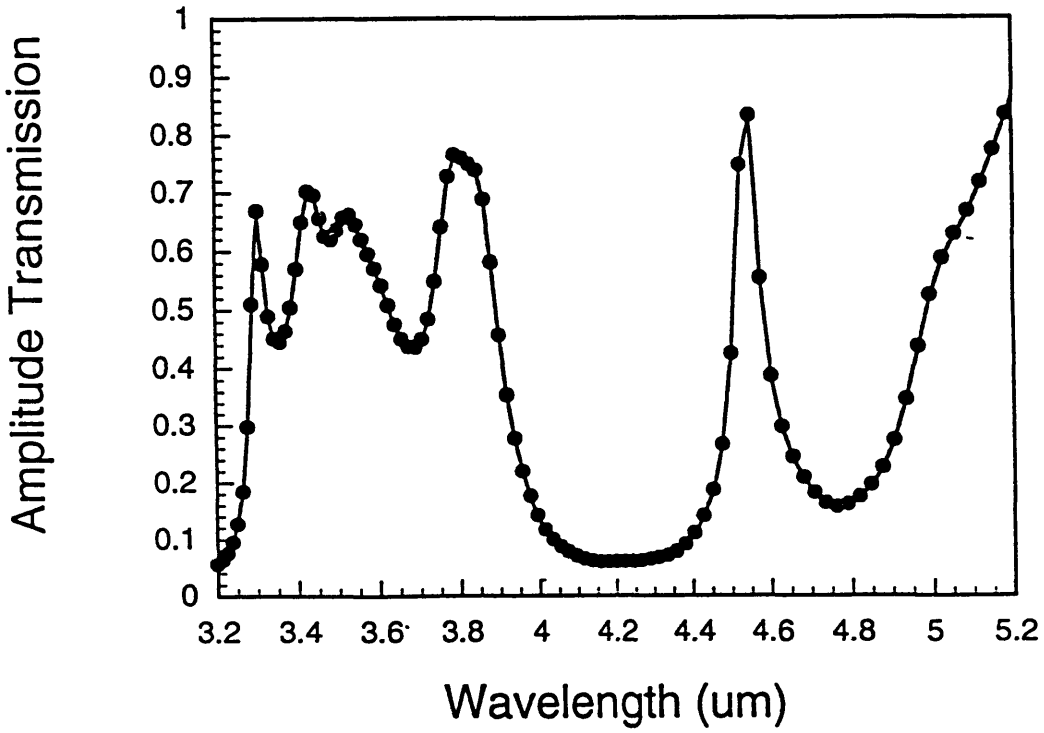

Figure 2-1. Wavelength response of the C1 bridge resonators.

2.2 Design of the coupling waveguides

From the bridge-resonator dimensions as given in Table 1, it is obvious that the structures are very small with respect to the design wavelength. An important issue arises when one considers doing experiments on these structures. Laser light has to be efficiently coupled and to do that one has to use strongly focusing optics at the input. The smallest focus spot size that can be achieved, is limited by diffraction and lens aberrations. In the ideal case that diffraction limited performance is achieved, the diameter of the focus spot d is approximately (Gaussian beam profile and paraxial approximation) given by :

$$d = \frac{4\lambda}{\pi} \cdot \frac{f}{D} \qquad (2.1)$$

where λ is the wavelength, f the focal length of the lens and D the diameter of the lens that is illuminated by the optical beam. Assuming that one illuminates all the lens area with still diffraction limited performance, the best one can get in practice is an f/D=0.5 (corresponds to a numerical aperture equal to 1 for the optic) which means that $d_{min} \sim 2\lambda/\pi$. For the wavelength of 4.5 microns this gives a $d_{min} \sim 3\mu m$. In practice one achieves much larger spots due to aberrations, nonvalidity of the paraxial approximation and actual numerical apertures smaller than 1. Even in this ideal case, however, the 3 micron spot size is still larger than the 1.6x0.4 micron bridge. The problem becomes more serious when one considers practically attainable spot sizes. Using near diffraction-limited reflective microscope objectives one can achieve (see Chapter 4) a 15μm spot with the 0.4 numerical aperture objective or a 12μm spot with the 0.5 numerical aperture optic in the best of cases. It is clear that one has to somehow match this large spot size with the bridge's small dimensions. To accomplish that, we design two tapered waveguides on either side of the bridge. The waveguide dimensions get gradually smaller from 15μm at the input down to the bridge dimensions at the bridge. We use two waveguides for coupling in and out from the resonators. Because it is very difficult to actually fabricate a vertical taper, we have only a horizontal taper. In the vertical direction the waveguide is 0.4μm thick (the same as the bridge).

Having the taper in the horizontal direction only, gives us a lot of troubles. First, the waveguide eigenmode will be strongly elliptical at the input which means significant coupling losses from

the circular focused laser spot there. Second, it is almost certain that the waveguide will be multi-mode in the horizontal direction, which means that one has to be extremely careful to excite the first order eigenmode. Exciting eigenmodes with the wrong symmetry would cause complete loss of power at the waveguide-bridge interface. Furthermore, the taper has to be smooth to avoid propagation losses along the waveguide. We choose the waveguide length to be 2mm (on either side).

Another important consideration, from the experimental point of view, is to distinguish the useful (guided) light at the output from light that is not coupled into the structures and diffracts or scatters in all directions. Considering the smallness of the structures, this is a serious problem. To make things easier, we design the waveguides bent on both sides to direct the guided beam in a different direction from the background radiation that goes straight. A schematic overview of the structure is shown in Figure 2-2. In calculating the bend angle, we take into account the diffraction angle of the focused spot at the input, the mechanical limit imposed by positioning the large microscope objectives and the fact that a reasonable number of devices has to be built on a particular sample due to the possibly limited yield of the fabrication process.

Ideally we would like to have the output guided beam out of the diffraction cone of the focused laser beam at the input. Recall that due to the elliptical shape of the waveguide mode at the facet, part of the circular focused beam will continue to propagate above the sample diffracting. From diffraction theory for Gaussian beams the cone's half-angle is given by $\theta_{dif} = \lambda/\pi w_o$, where w_o is the radius of the focused spot and λ the wavelength. For λ=4.5 and w_o=7 microns we find that θ_{dif} ~ 11 degrees. Now, there is an effective angle $\bar{\theta}$ associated with the position where we have placed our aperture to isolate the guided beam at the output (see Figure 2-3a, b). If our bending angle is θ, we also have a choice to cut the facets of the sample perpendicular to the waveguides or not. In the second case, the beam will enter and/or exit the sample at the angle dictated by Fresnel's law $\phi = \sin^{-1}(1/n_{eff})$ ~ 20 degrees, where n_{eff} is the effective mode index of the waveguide at the input (approximately 2.9, see calculations below). This case is shown in Figure 2-3b. If the aperture distance from the output facet of the sample is z and s=2mm is the length of each of the waveguides,

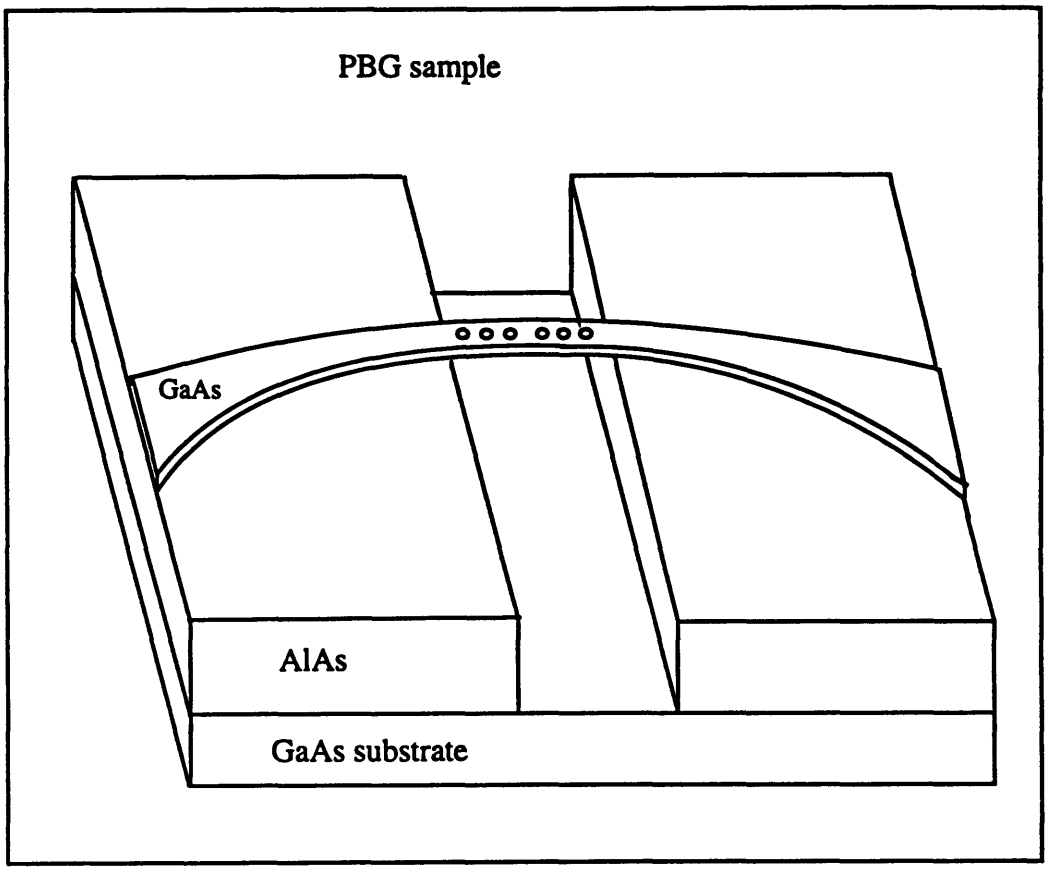

Figure 2-2. Scematic overview of the structure with the waveguides.

then $\overline{\theta} = \theta + \theta'$ where θ' is given by :

$$\theta' = \text{atan}\left(\frac{z}{z+2s}\tan\theta\right) \qquad (2.2)$$

for the case that the output facet is cut (Fig. 2-3a) ,

$$\theta' = \text{atan}\left(\frac{n_{eff} z \sin\theta}{z\sqrt{1-n_{eff}^2(\sin\theta)^2}+2s\cos\theta}\right) \qquad (2.3)$$

in the case that the output facet is not cut (Fig. 2-3b).

The necessary condition to avoid the diffraction cone at the aperture position is $\theta+\theta'>\theta_{dif}$ if the input facet is cut and $\phi+\theta'>\theta_{dif}$ in the case that the input facet is not cut. When both sides are cut, the condition is satisfied for $\theta>5.5$ degrees assuming that z~the working distance of the collecting objective (14.5mm). In the case that the input facet only is cut, the same condition holds for $\theta>3.5$ degrees (smaller due to the additional Fresnel refraction) and when only the input facet is cut for $\theta>3$ degrees. Finally, when both facets are not cut, the condition is true for $\theta>2$ degrees.

On the other hand, the large dimensions of the objectives impose a restriction on θ by themselves. Taking into account that their diameter is D_1~D_2~40mm and their working distances are w_1=14.5mm and w_2=8.6mm the necessary condition is (Figure 2-4) :

$$\frac{D_1}{2}\sin\theta_1 + \frac{D_2}{2}\sin\theta_2 \le w_1\cos\theta_1 + w_2\cos\theta_2 \qquad (2.4)$$

when a facet is cut perpendicular to the waveguide $\theta_i=\theta$, whereas when is not cut $\sin\theta_i=n_{eff}\sin\theta$. It turns out that the above condition is satisfied for $\theta < 30$ degrees when both sides are cut, $\theta < 12$ degrees when only the output facet is cut and $\theta < 8$ degrees when no facet is cut. Another restriction on θ comes from the total internal reflection angle. When the output facet is not cut θ has to be smaller than $\text{asin}(1/n_{eff})$=20 degrees, otherwise the guided mode will be totally reflected at the output facet! We also mention here that the Brewster angle is 19 degrees, very close to the total internal reflection angle. It would therefore be dangerous to aim for the Brewster angle at the output facet of the sample. Considering all the above cases and restrictions, the useful range for θ is

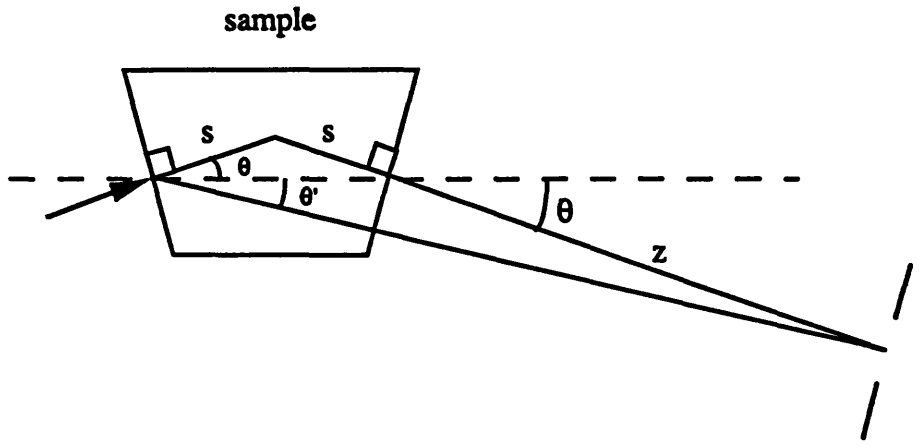

(a)

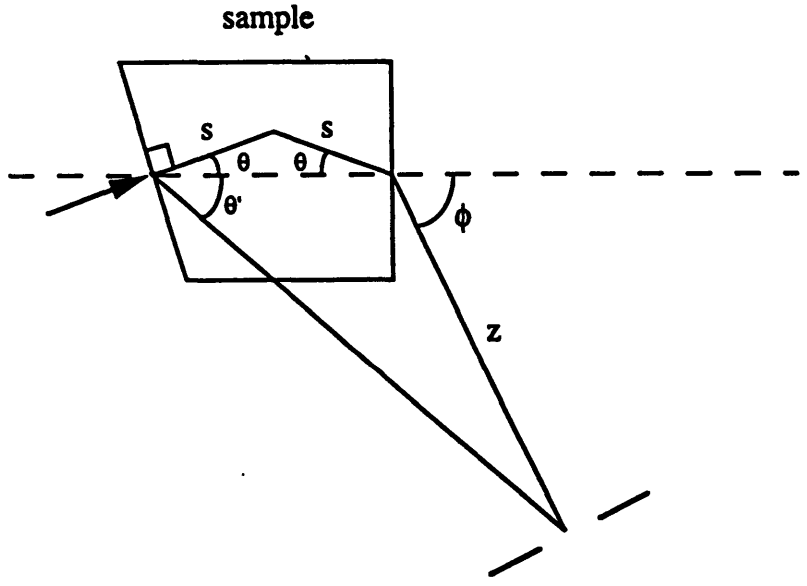

(b)

Figure 2-3. Coupling geometry when the output facet is cut (a) and not cut (b).

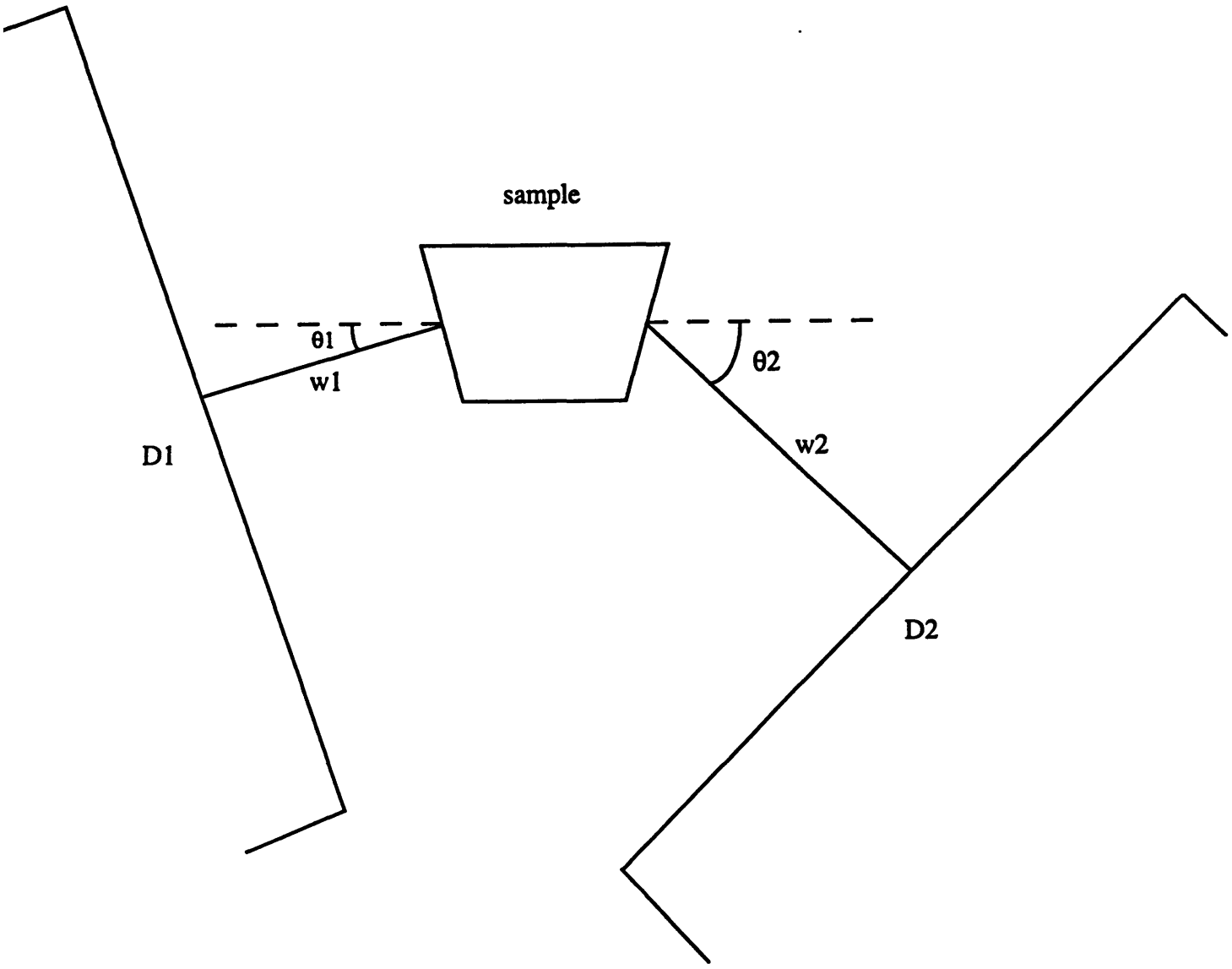

Figure 2-4. The coupling and collimmating objectives geometry.

between 5.5 and 8 degrees. We assume here, that there are no specific requirements about whether any of the facets will be cut or not. Our choice was a bending angle θ=6 degrees for both waveguides.The radius of curvature R is approximately equal to $2\cot\theta \sim 19$mm pretty large to ensure ease of fabrication and a smooth waveguide bend.

The most important issue related to the waveguides is what their eigenmode is at the input (or output) facet and at the bridge. This determines the total coupling efficiency of laser light into the structures. The factors that affect the eigenmodes are first the materials used and second the cross-sectional structure of the waveguides. Regarding the materials, we use 0.4 μm thick GaAs (n=3.3) layer for the waveguiding layer (same as for the bridge). For the substrate we first consider an AlAs (n=2.85) layer. To find the waveguide eigenmodes we use a beam propagation method (BPM) code developed by Jerry Chen [16]. This program finds the first and higher order waveguide eigenmodes through beam propagation along the imaginary axis and calculates overlap integrals between field distributions (for example eigenmodes, Gaussian beams). One can also simulate real propagation along a waveguiding structure. Starting with just a 0.4 μm thick GaAs layer on top of an AlAs substrate, we see that there is a mode at the input (GaAs 15μm wide), but it lies well into the substrate (Figure 2-5a). In the Figure we assume that the guiding structure has been etched by 1 micron on the sides. This happens during the fabrication process. At the bridge where the guiding layer is much narrower (1.6μm) there is no mode. Everything has radiated into the substrate. To bring the mode higher into the GaAs layer, we use an $Al_{0.3}Ga_{0.7}As$ (n=3.1) overlayer on top of GaAs. An $Al_{0.7}Ga_{0.3}As$ underlayer (n=3.05) is also grown to make things more symmetric. For example, the abrupt index change between the AlAs substrate and the guiding layer might in fact cause the mode to go higher up into the overlayer. We now see that we have a well-centered mode at the input regardless of the overlayer thickness (see Figure 2-5b with over- and underlayer thicknesses of 0.2μm). But at the bridge a relatively thick overlayer (over 0.8μm) is needed for a mode to appear (Figure 2-5c). A solution would therefore be to use a 0.8μm overlayer all along the waveguide up to the bridge. The reason for not doing this is serious concern about the existence of higher order modes in the vertical dimension. This would be a disaster for coupling into the bridge. We therefore prefer to stay with the 0.2-0.4-0.2μm $Al_{0.3}Ga_{0.7}As$-GaAs-$Al_{0.7}Ga_{0.3}As$ structure and instead of a thicker overlayer we are going to oxidize the AlAs substrate to a depth (and side-ways penetration) of 1μm. Close to the waveguide-bridge interface this

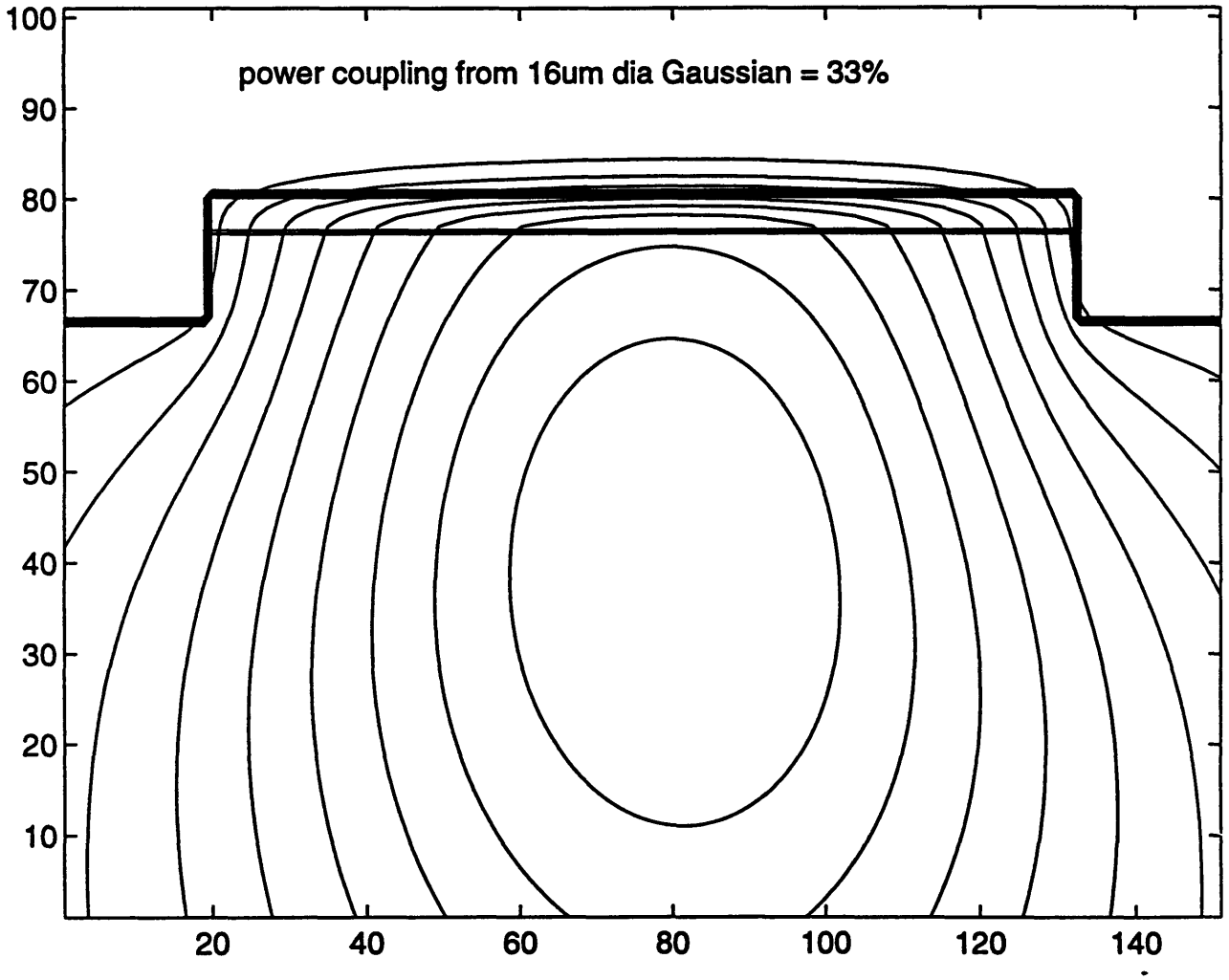

Figure 2-5a. The eigenmode at the input of the waveguide when there is no overlayer. The window dimensions are 20x10 microns.

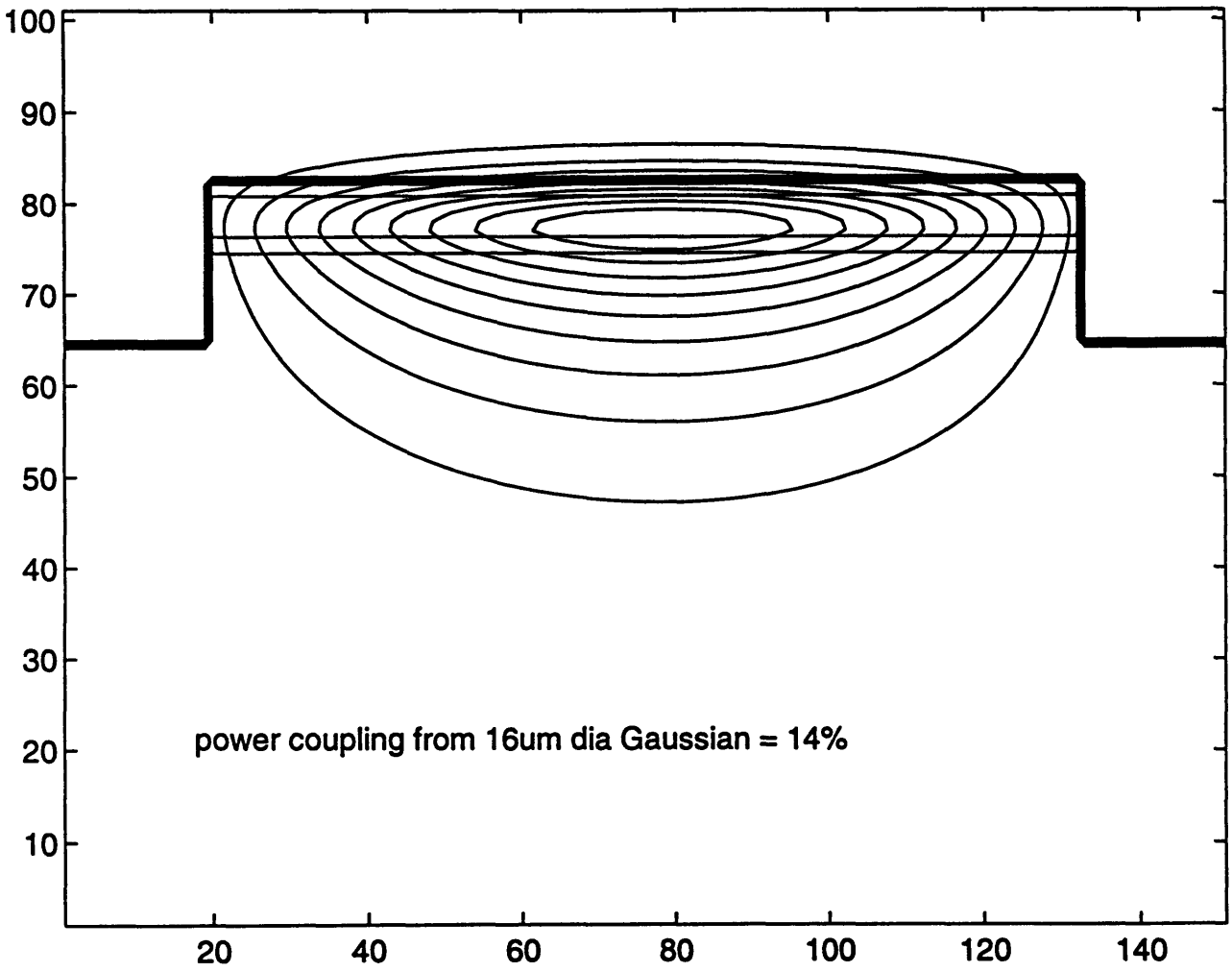

Figure 2-5b. The eigenmode at the input of the waveguide with a 0.2 micron overlayer. The window dimensions are 20x10 microns.

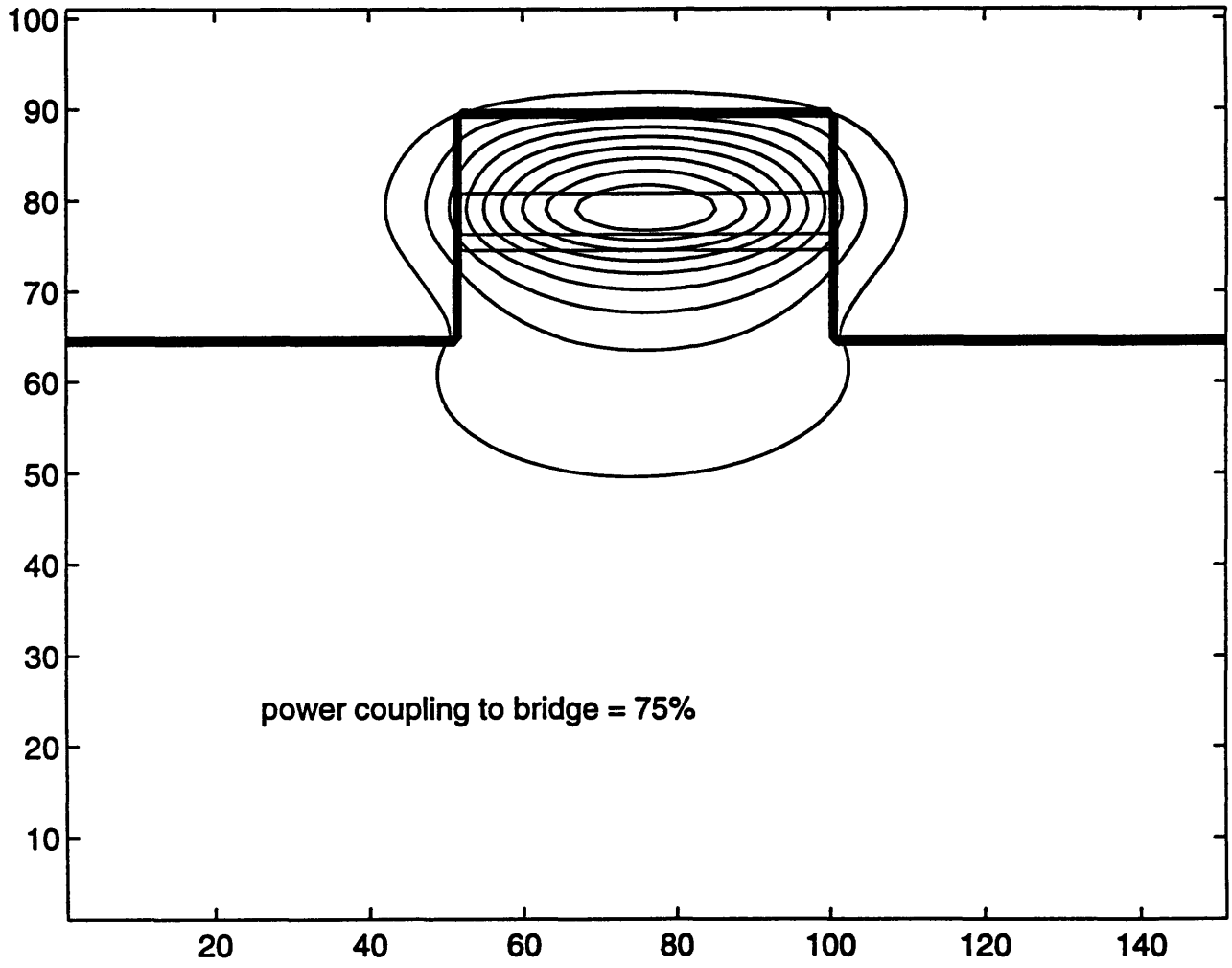

Figure 2-5c. The eigenmode at the input of the waveguide with a 0.8 micron overlayer. The window dimensions are 5x10 microns.

is enough to fill the entire space underneath the underlayer with oxide. Al_2O_3 has a very low refractive index (1.55) and this gives a very nice mode centered at the GaAs guiding layer resulting in 98% power transmission into the bridge mode! In Figure 2-6 we present this along with the bridge eigenmode, the waveguide eigenmode at the input (with an effective index of 2.906) and at a distance 0.5mm before the bridge. The coupling efficiency from a 16μm diameter Gaussian beam at the input is ~10%. Taking into account the ~60% transmission through the resonator and the ~76% transmission at each of the facets due to reflection losses from normal incidence, we theoretically have a 3% (!) overall transmission through the entire structure.

2.3 Fabrication

As mentioned earlier, the photonic bandgap air-bridge is grown using GaAs and GaAlAs alloys. The initial compound semiconductor material for the photonic bandgap air-bridge structure is grown by gas-source molecular beam epitaxy. A series of high-resolution photolithography, reactive ion etching and wet chemical etching steps are then performed to fabricate the bridge and waveguide structures. On each sample three groups of seven curved waveguides each are grown. The top and the bottom structures in each group have bridges with no holes, whereas the other five have resonators with holes corresponding to the C1, C2 and C3 structures of Table 1 (one structure per group). The structures with no holes are made with the purpose of testing the coupling into the waveguides first, before going on with the actual bridge response measurements. Apart from the curved waveguides, some resonators coupled to straight waveguides are grown. A picture showing one such photonic bandgap air-bridge fabricated by K.Y. Lim, G. Petrich in Prof. L.A. Kolodziejski's group is presented in Figure 2-7.

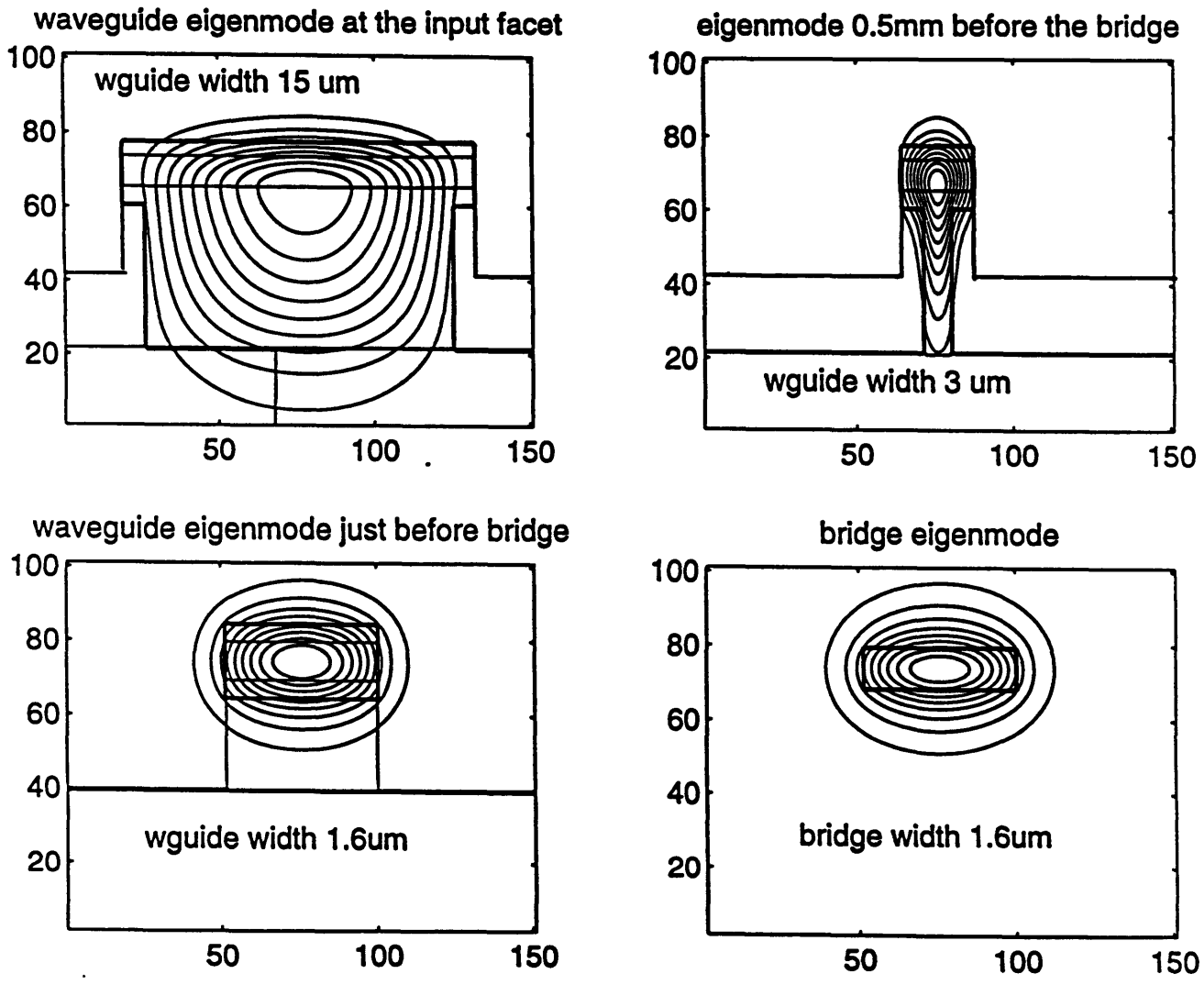

Figure 2-6. Waveguide eigenmode at various positions for the final structure. The window dimensions are 20x5 microns for the two upper figures and 5x4 microns for the lower two figures.

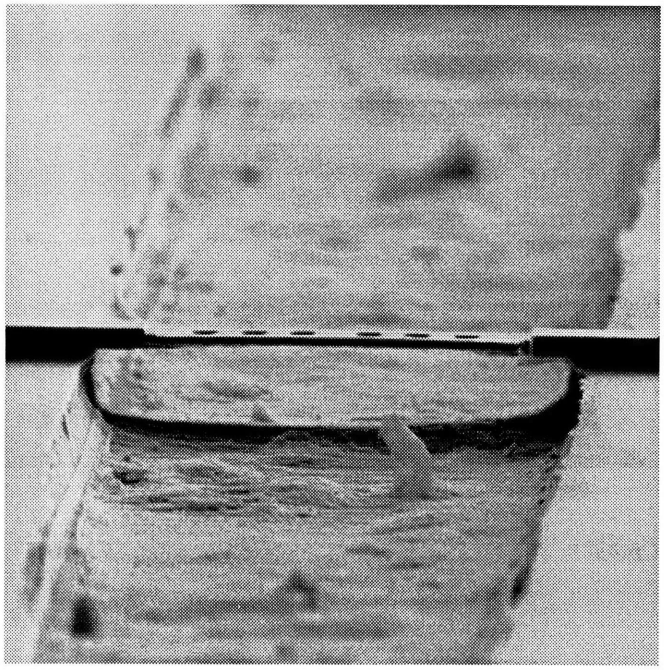

Figure 2-7. SEM photograph of the air-bridge resonator. The defect, three holes on either side and the overlayer (etched away at the bridges) can be clearly seen (Courtesy of Kuo-Yi Lim, Prof. Kolodziejski's group).

Chapter 3

The experimental setup

In this chapter we describe the experimental setup that is developed to study the photonic bandgap air-bridge devices. In the first paragraph a general description is given and in the second paragraph we present the basic principles behind the optical parametric oscillator used. In the last paragraph the difference frequency generating stage is described.

1.1 General

To characterize the spectral response of the photonic bandgap air-bridge a coherent, widely tunable infrared femtosecond source in the 3 to 5 micron range is needed. The wide tunability is needed to be able to move over the entire range of the bandgap. Femtosecond pulses provide the wide spectrum that allows single-shot measurement of the cavity resonance. An Optical Parametric Oscillator is used as a source. It is pumped by a mode-locked Ti:sapphire laser and produces two femtosecond pulse trains (signal and idler) in the near infrared (1.1 to 2.25 microns) wavelength range. To produce pulses at the longer wavelengths from 4 to 5 microns needed for this experiment, a difference frequency generating stage follows. The signal and idler pulses are combined to give the difference frequency femtosecond pulses which are then coupled into the samples. The light that comes out from the structures is guided into a spectrometer for a scan of the device response versus wavelength. A schematic overview of the experimental setup is shown in

Figure 3-1.

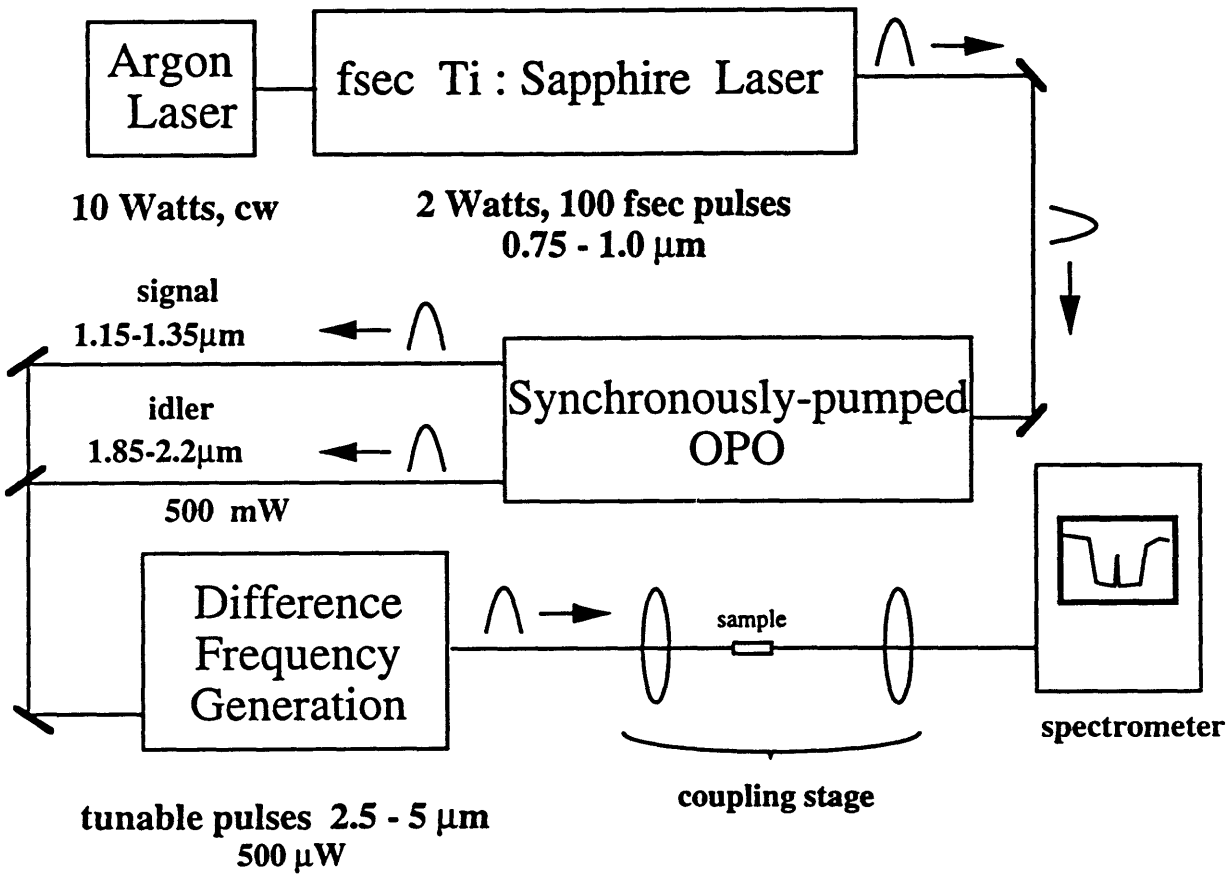

Figure 3-1. Scematic overview of the experimental setup.

3.2 The Optical Parametric Oscillator

Optical Parametric Oscillators (OPOs) are sources of coherent radiation with many desirable characteristics. Their operation is based on parametric interaction in a nonlinear $\chi^{(2)}$ crystal placed inside a cavity. More specifically, a laser beam (pump) at frequency ω_p is directed into the nonlinear crystal. Through parametric generation, two optical beams (signal and idler) at frequencies ω_s and ω_i are produced such that $\omega_p = \omega_s + \omega_i$. When the OPO is synchronously pumped by a train of pump pulses, ultrashort pulse generation for both the idler and the signal fields can be achieved. The crystal is placed inside a cavity which can be resonant for the signal only (singly resonant cavity) or for both the signal and the idler (doubly resonant cavity). In a singly resonant cavity, the generated signal pulses travel back and forth inside the resonator and mix with the pump pulses in the crystal reinforcing the nonlinear generation process (Figure 3-2). At steady state, three pulse streams are obtained at the output, that is, the signal, idler and what is left from

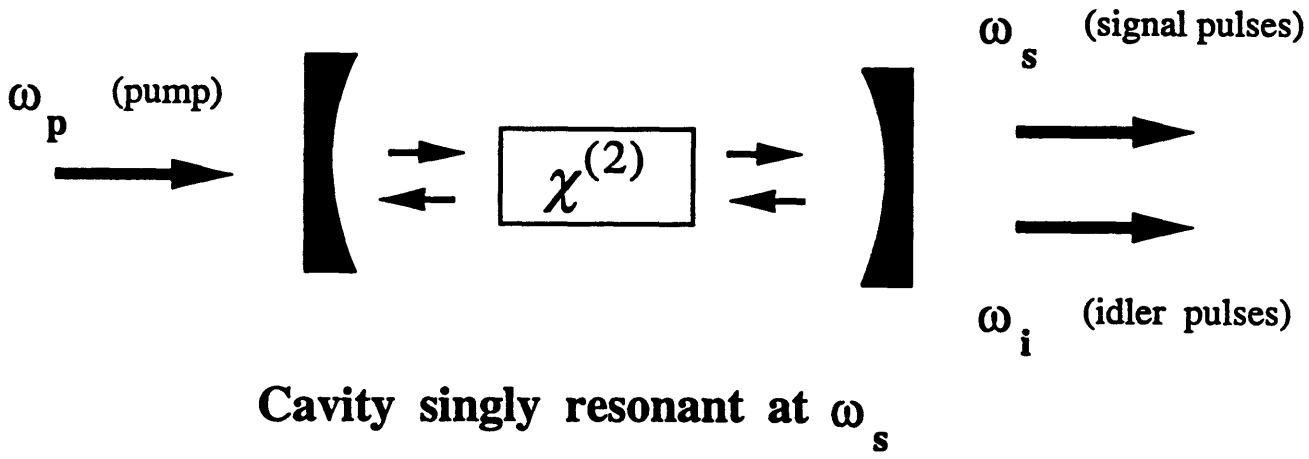

Figure 3-2. An Optical Parametric Oscillator cavity.

the pump. There are two very important issues involved in the whole process. The first is phase matching or momentum conservation. In order to achieve efficient parametric generation inside the crystal, the total momentum of the photons participating has to be conserved. This can be also expressed as $\mathbf{k}_p = \mathbf{k}_s + \mathbf{k}_i$ or $n(\lambda_p)/\lambda_p = n(\lambda_s)/\lambda_s + n(\lambda_i)/\lambda_i$, where n is the refractive index of the crystal which is wavelength and temperature dependent. For birefringent materials, as is usually the case for crystals used in OPOs, n depends also on the orientation of the crystal with respect to the optical beam polarization. One can achieve phase matching for many different triads of wavelengths and polarization of beams by either varying the orientation of the crystal (critical phase matching) or changing the temperature of the crystal (noncritical phase matching). The wide tunability of the OPO stems from the ability to achieve phase matching for a large wavelength range (often limited by the crystal transparency range). The second important issue is synchronicity. This means that the pump and the resonant (signal) pulses have to enter the crystal at the same time. To ensure this, the OPO cavity length has to exactly match that of the pump laser source (Synchronously Pumped Parametric Oscillators (SPPOs)). It should be mentioned here, that there is a threshold pump power required to achieve OPO operation. To reach steady state oscillation, one has to have parametric gain high enough to compensate for losses due to cavity mirror transmission, reflections at the crystal surfaces, crystal absorption and losses due to diffraction. Designing an optical parametric oscillator is a difficult task as one has to take into account many other important effects that can take place inside the cavity [18], [19].

The development of ultrafast optical parametric sources with excellent characteristics has been closely related to the advent of the mode-locked Ti:sapphire laser and new improved nonlinear optical materials. First with synchronously pumped dye lasers and then by continuum generation and optical parametric amplifiers, widely tunable synchronized pulses were demonstrated. SPPOs provide an alternative way with the advantage of greater simplicity (all solid-state, directly pumped), higher pulse repetition rates and lower noise with respect to the other sources. In addition, tunability, the availability of synchronized femtosecond pulses simultaneously at multiple wavelengths, spatial mode quality and reasonably high average and peak power pulses make these sources very attractive for performing ultrafast spectroscopy experiments. For more information on recent developments the reader is refered to [20] and [21].

In our experiment we use an optical parametric oscillator commercially available by Spectra Physics (OPAL). This system uses a Ti:sapphire laser as a pump source. Ti:sapphire is pumped by

an Argon laser and gives out 100fsec pulses with average power around 2W (with 12W Argon power) at wavelengths between 720 and 850nm. The repetition rate of the pulses is 80MHz and this actually determines the OPO cavity length. Before entering the OPO, the Ti:sapphire pulses pass through a half-wave plate to rotate their polarization to be vertical with respect to the table. In Figure 3-3, the OPO cavity is shown. The nonlinear crystal used for the parametric conversion is lithium borate (LBO) which can be both noncritically phase-matched and temperature tuned over a large wavelength range. These are important advantages especially for the construction of a commercially available optical parametric source [19]. First, noncritical phase-matching offers maximum nonlinear coefficient and absence of walk-off. Also, the pump beam overlaps with the signal beam; and, therefore, alignment of the cavity with the more convenient pump beam is possible. On the other hand, T tuning is ideal for constructing a system that does not require realignment every time the wavelength is tuned because the crystal orientation remains fixed. It should be noted here, that the signal and idler polarizations at the output of the OPO are both horizontal with respect to the table surface (Type I phase-matching).

The OPAL cavity is singly resonant for the signal and has a total length of 1.87m (80MHz repetition rate). It basically consists of two curved mirrors to focus into the crystal. An additional curved mirror is used to collimate the idler which is then guided out of the cavity. For fine cavity length control, a motor-controlled output coupler is employed for the signal and a piezoelectric transducer is attached to one of the intracavity mirrors. Both these mirror positions and the crystal temperature are controlled by a microprocessor. More details on the OPAL system described here can be found in Reference [19].

Tuning is accomplished by adjustment of the crystal temperature and optimization of the cavity length. Two sets of optics can be used in the OPAL. The first one (1.3μm set) covers the range of 1.10 to 1.35μm for the signal (idler from 1.80 to 2.25μm) and the second one (1.5μm set) from 1.33 to 1.60μm for the signal (idler from 1.64 to 2.06μm). The numbers given here correspond to a 775nm pump. In the OPAL system we have in our laboratory the 1.3μm set is used. Average powers for the signal and idler pulses are shown in Figure 3-4 and range in general from 100 to 400 mW for the signal and up to 200 mW for the idler. The system is constructed so that the total path length traveled by the signal and idler pulses, as they come out from the crystal to the output, are the same. Therefore, synchronization between the signal and idler pulses is expected to be very good.

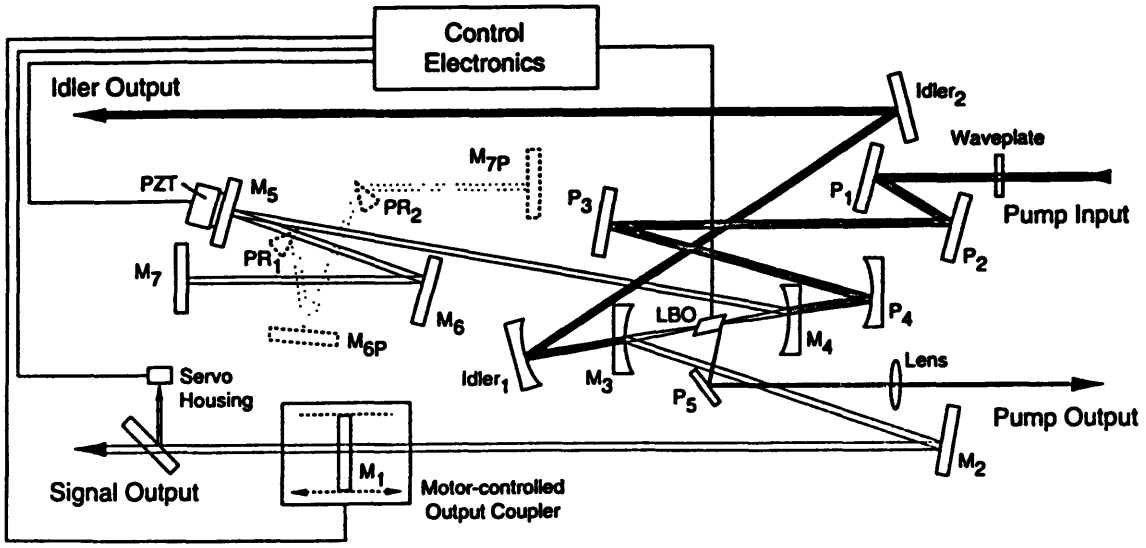

Figure 3-3. Schematic overview of the Ti:sapphire-pumped SPPO. P_1-P_5 are pump mirrors, M_1-M_7 are cavity mirrors, and PR_1-PR_2 are intracavity Brewster prisms. M_{6P}-M_{7P} are cavity mirrors used when the intracavity prisms are inserted. PZT is a piezoelectric transducer (from Ref. [19]).

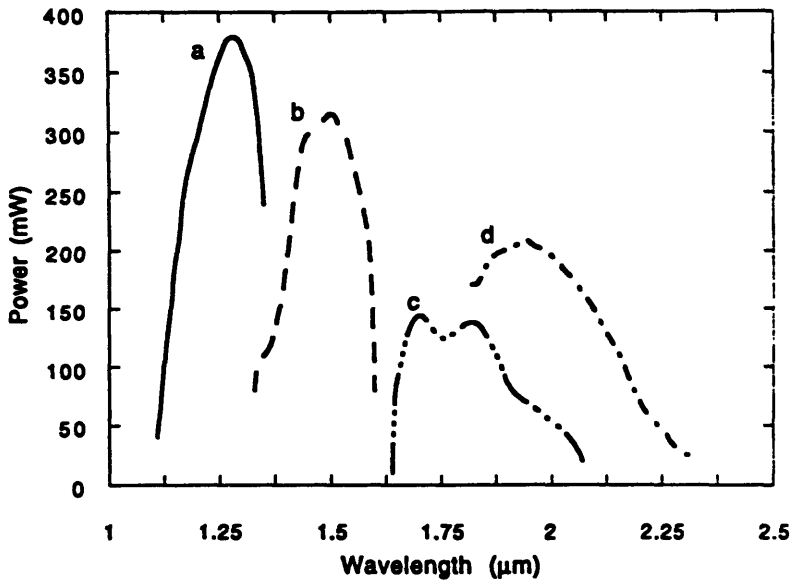

Figure 3-4. Typical output powers from the Ti:sapphire pumped OPO as a function of the wavelength (from Ref. [19]).

3.3 The Difference Frequency Generation stage

The purpose of the Difference Frequency Generation (DFG) stage is to coherently combine the signal and idler pulses coming out from the OPO to produce femtosecond pulses tunable at the longer wavelength range needed for the study of the photonic bandgap air-bridges. The wavelength conversion is again achieved through a nonlinear parametric process inside a crystal. Photons at the signal frequency ω_s combine with photons at the idler frequency ω_i to produce photons at the difference frequency $\omega_d = \omega_s - \omega_i$. For the conversion to be efficient, phase matching has to be achieved inside the crystal. The condition for that can be written as $\mathbf{k}_d = \mathbf{k}_s - \mathbf{k}_i$ or $n(\lambda_d)/\lambda_d = n(\lambda_s)/\lambda_s - n(\lambda_i)/\lambda_i$, where n is the refractive index of the crystal. Depending on the polarization of the beams and the orientation of the birefringent crystal, one can satisfy the phase-matching condition continuously over a wide frequency range for the difference. The closer the signal and idler

frequencies are, the longer the generated wavelengths.

Generation of infrared femtosecond pulses has been demonstrated in the past using amplified dye-laser systems [22], [23], and various other techniques using a Ti:sapphire laser [24-26]. More recently, an OPO synchronously pumped by a Ti:sapphire has been used to generate fsec pulses in $LiNbO_3$, $LiIO_3$ and $AgGaS_2$ crystals tunable in the 2.5 to 5.3 microns range with powers up to 400 μW [27-30]. In comparison with the previous schemes, the latter one offers higher powers, better pulse stability and higher repetition rate for the difference pulses at the same time. What makes a SPPO attractive for generation of pulses at longer wavelengths is its ability to provide synchronized subpicosecond pulses simultaneously at multiple wavelengths and the relatively high average powers achievable for the signal and idler pulses.

The experimental setup we are using does not difer much from the configurations presented in the above papers. The setup is shown in Figure 3-5. We use a 1mm long lithium iodate $LiIO_3$ crystal. We use type-I phase-matching where the signal is polarized along the extraordinary axis direction and the idler and difference frequency along the ordinary axis. The crystal is mounted so that its ordinary axis is in the horizontal direction and this gives difference frequency pulses with the desired orientation for coupling into the bridges. Recall that the bridge resonator eigenmode is TE-like having its electric field polarized in the horizontal plane. The calculated phase-match angle and walk-offs between the signal-idler, signal-difference and idler-difference pulses inside the crystal are shown in Figures 3-6 and 3-7 respectively. Note that the 3.5 to 5 micron wavelength range tuning is achieved for rotation of the crystal in a 2 degree range. Also the temporal walk-off between the signal, idler and difference pulses will result in longer than 100fsec pulses for the difference frequency. Since the walk-offs do not exceed the 250fsec/mm value, a 1mm long crystal is expected to generate difference frequency pulses less than 250fsec long in duration. In order to rotate the polarization of the signal pulses a half-wave plate for the 1.3micron wavelength is used. A delay stage is employed to compensate for path length differences for the signal and the idler, which are then combined with a dichroic beamsplitter into one beam. Then they are collinearly focused onto the crystal. The resulting difference frequency and what remains from the signal and the idler are then collimated by another CaF_2 lens. Next, a Ge plate is used to block the signal and idler frequencies. The difference frequency pulses are then guided into a spectrometer (1 nm resolution) to determine the spectral shape of the pulses. In previous work on genera

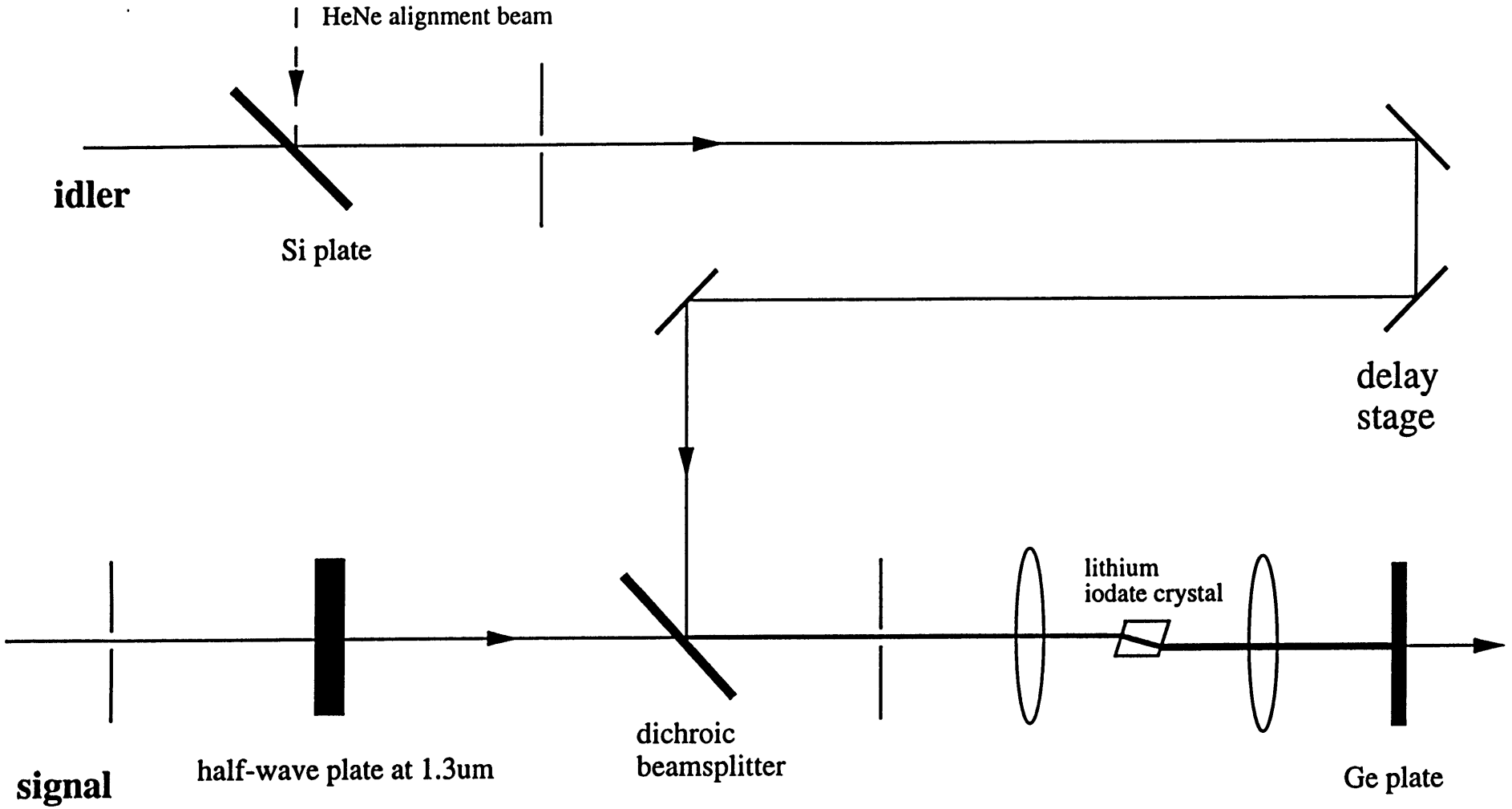

3-5. The difference frequency generation setup.

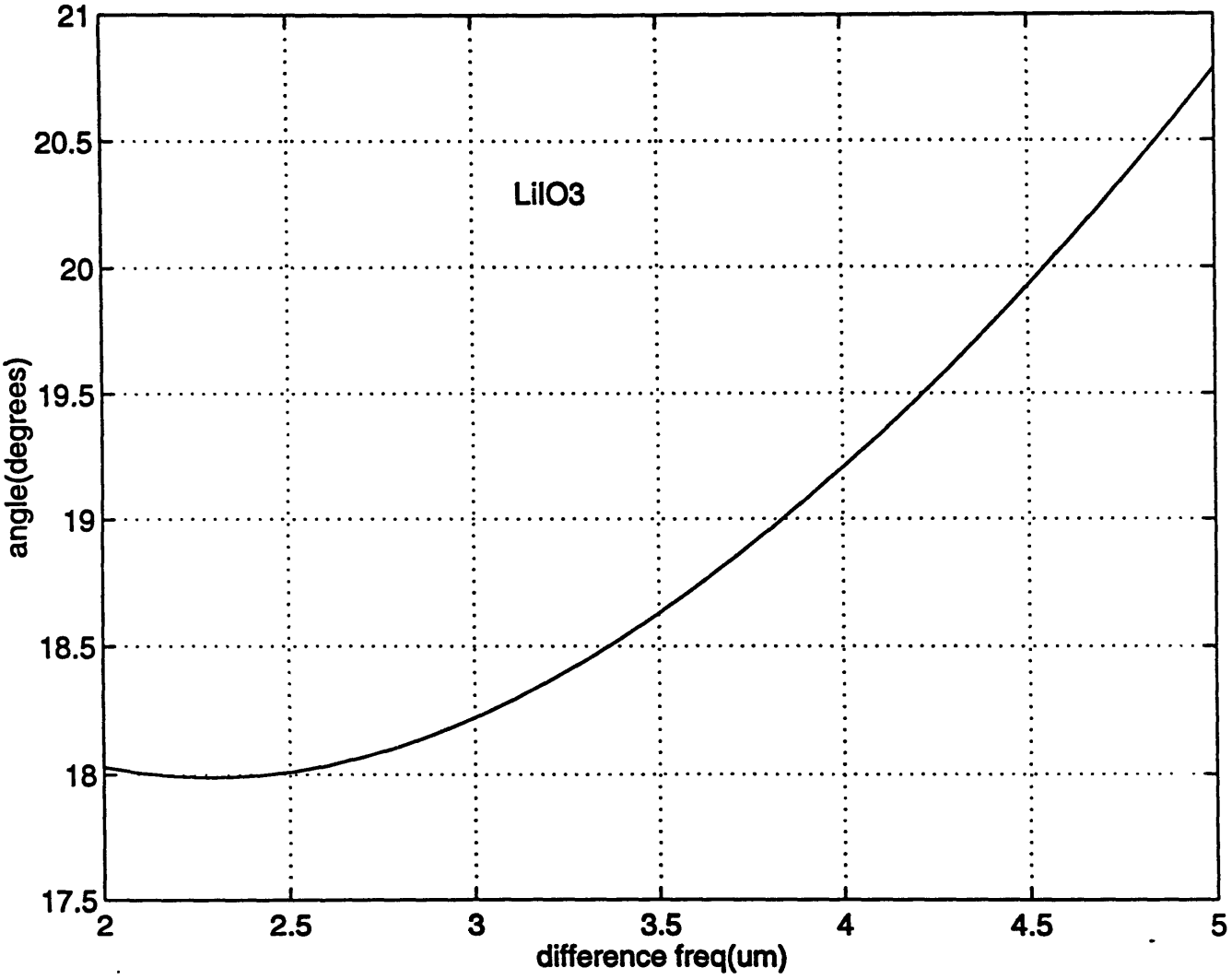

Figure 3-6. Type-I phase-matching angle for $LiIO_3$ as a function of the difference wavelength.

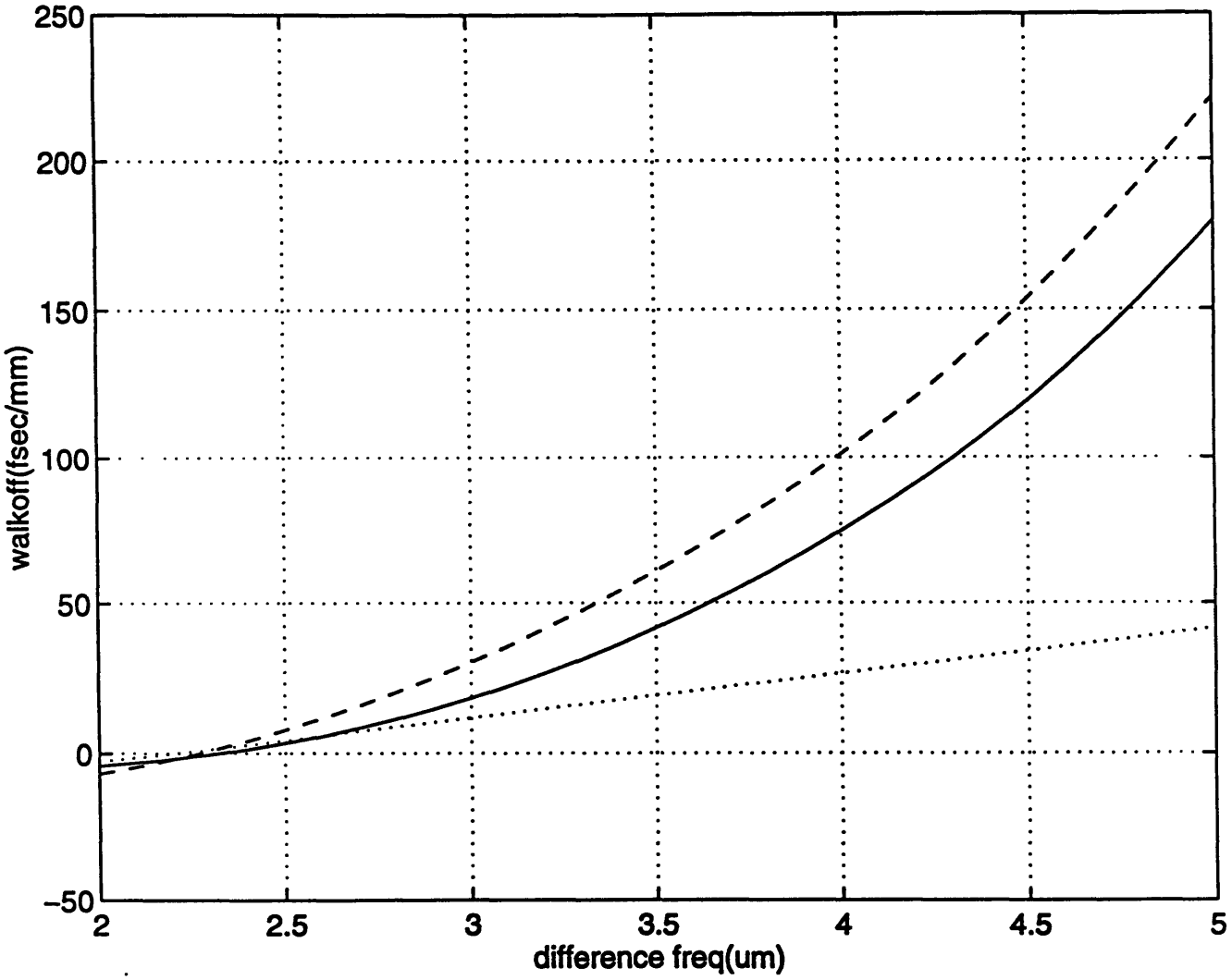

Figure 3-7. Walk-offs between the various pulses inside $LiIO_3$ as a function of the difference wavelength.

tion of tunable infrared pulses [29,30] the sum frequency was first obtained and the system was optimized more easily since the sum frequency is the same as the Ti:sapphire beam. Then just by rotating the half-wave plate the difference was generated without a need to tilt the crystal. Powers in the order of a few hundreds of μW were obtained. The spectrum of the generated pulses was around 170nm [29]. Just for comparison, the resonance width of an air-bridge with a Q of 46 centered at 4.55μm (C1 structure) is 99nm, almost two times smaller.

Chapter 4

The coupling stage

In this chapter the setup used to couple light in the waveguides is presented. The exact procedure followed to achieve coupling is described and some important issues regarding this experiment are mentioned.

4.1 The coupling setup

The experimental setup we use for coupling light into the structures is shown in Figure 4-1. To facilitate coupling, we use a 980nm laser diode beam and a helium neon (HeNe) beam. The 980 beam can go through the GaAs material and since it is visible with a CCD camera can be used for alignment to help direct the IR beam. The HeNe on the other hand makes everything a bit easier by providing a visible path. It is not absolutely necessary. These beams are combined with the infrared using a silicon plate which transmits infrared wavelengths above 1.2 microns and reflects the diode and HeNe. Notice the thin glass plate used to combine the 980 with the HeNe light. Glass does not completely reflect or transmit the HeNe and 980 beams and what is left is guided with some mirrors for coupling into the structures from the back side. The purpose of doing this is explained later. The entire setup is built on a 18x24 inch breadboard.

To focus and collimate light into and from the waveguide ends we use two reflective microscope objectives purchased from Ealing Electrooptics. Apart from exhibiting a near diffraction-limited

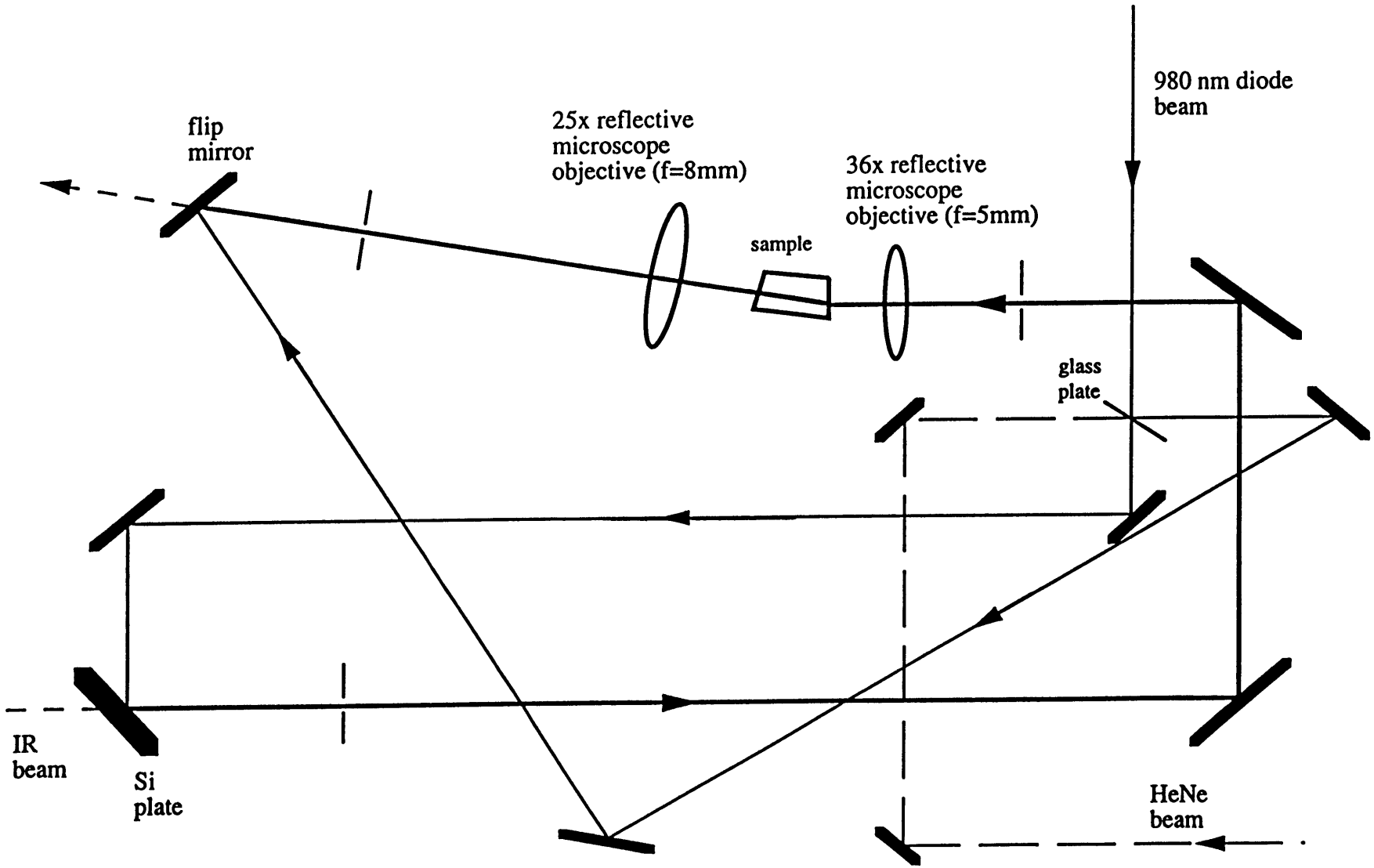

4-1. Experimental setup for coupling light into the air-bridges.

performance in an extremely wide wavelength range (from UV to far IR), the main reason for using these objectives, instead of ordinary refractive lens systems, lies in the fact that they are achromatic. They consist of two mirrors, a small convex one and a large concave. The small convex mirror expands the incoming beam to fill the surface of the large concave mirror, which in turn focuses radiation down to a very small spot (Figure 4-2). By choosing appropriate values for the mirror radii of curvature and their separation, it is possible to correct the primary spherical, primary coma and primary astigmatism aberrations. Due to the reflective nature of the configuration (absence of dispersive elements) the objectives behave achromatically from the ultraviolet to the far infrared! This means that the focused spots will always be at the same position regardless of the wavelength and the spectral content of the focused light. This is very important in our case, where we would like to know that the 980nm spot coincides almost exactly with the invisible 4.5 micron light spot. Furthermore, the particular geometry of the mirror system is responsible for the much larger working distances and numerical apertures that these objectives offer, in comparison with refractive ones, at the same time. The only drawbacks of these objectives are their relatively large size and the fact that the small mirror represents an obscuration to the focused light. This

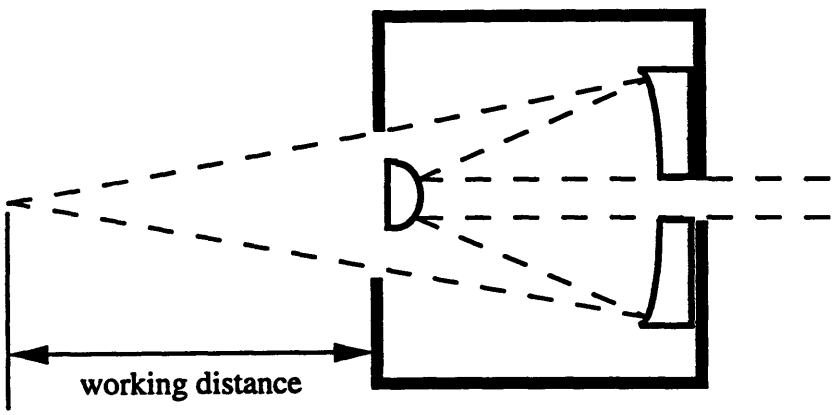

Figure 4-2. The construction of a reflective microscope objective.

results in some nonnegligible loss of power especially with beams of nonuniform irradiance profile (e.g. Gaussian). It also modifies the classical Airy pattern, by making the central spot smaller and the outer rings slightly brighter. In order to achieve the highest throughput and smallest spot size possible, care should be taken so that the incoming beam diameter matches the diameter of the small mirror. The focusing objective in our setup has a NA of 0.5, focal length 5.4mm and a working distance of 8.6mm. The obscuration losses are 12.2% and refer to uniform illumination. The small mirror diameter is 5.6mm. The collimating objective has NA 0.4, focal length 8mm, working distance 14.5mm and obscuration losses of 16.7%. Its small mirror diameter is 6.3mm. The minimum spot sizes achievable at the wavelength of 5μm are ~12μm for the first one and ~15μm for the second. This assumes uniform beam intensity and does not take account of the secondary maxima [31].

The sample is cut on both sides so that the facets are perpendicular to the waveguides. This makes it easier to orient the bulky focusing optics in the setup so as to be roughly at the right coupling angle. In addition, it leaves more space to accomodate the bulky focusing optics and their mounts. Recall from Chapter 2 that other options would be to leave the sample uncut on either one or both sides. As regards coupling in, this would require coming with the focused spot at the Fresnel angle (approx. 20 degrees) which is not a trivial task when orienting the large microscope objectives. Furthermore the Fresnel angle is wavelength dependent meaning that using the 980nm beam to help coupling the infrared one, would not be particularly useful. At the output facet, however, the fact that the guided beam emerges at an even larger angle could be useful to separate the guided light from background radiation. We consider this later on. Fine micropositioning equipment is needed to be able to move the sample by extremely small intervals in order to optimize coupling. The sample is mounted on a xyz piezotranslator configuration which allows for submicron movement in all three directions (horizontal, vertical and focus adjustment). In addition, a goniometer is used for better control of the two azimuth angles ϕ and θ. A Bausch&Lomb stereoscope with a CCD camera attached on it is used to look at the sample from the top. This will help determining whether the 980nm light has been coupled in. The maximum magnification of the microscope in this configuration is a factor of 7.

4.2 Coupling light into the structures

The coupling experiments were performed in the MIT Spectroscopy laboratory using a lead-salt diode emitting cw radiation at around 4.8μm. A 63mm focal length CaF_2 lens is used to collimate the diode light. The procedure to couple light into the structures is as follows. Using an Electrophysics pyroelectric infrared camera and a room temperature PbSe detector, we first guide the infrared beam through the Si plate and the two irises (Figure 4-1). We try to have the irises spaced as far apart as possible and we take care that the infrared beam is level. Then we coalign the 980nm and the HeNe beams using a pair of mirrors and a glass plate. Using another pair of mirrors we combine these two beams with the infrared using the Si plate and the irises. After the second iris we look at the beams far away to make sure they really overlap. This is needed because the infrared beam diameter is pretty large and it is not certain that the two-iris method automatically guarantees perfect alignment. Then we place the focusing objective in the beam path taking care that the beams hit the small mirror centered as much as possible. The 980nm and HeNe beams are expanded using two lenses by a factor of 3 in order to match the mirror diameter. Next, we place a 15μm pinhole in front of the objective and pass all three beams (especially the infrared and the 980) through it. We measure the infrared (4.8μm) focused spot size using the pinhole and imaging it onto the InSb detector using the f=8mm objective. A Klinger stepper-motor is used to translate the focusing objective in 0.1μm steps in the horizontal direction. A Burleigh piezoelectric translator moving by 300nm per Volt is used for the vertical direction. A short program was written to do scans with the stepper-motor and take real-time data. The spot profile in the horizontal direction is shown in Figure 4-3 where the horizontal scale is in 0.1μm units. The profile fits to quite well to a Gaussian with ~18μm 1/e width. Assumming a Gaussian shape, deconvolution with a 15 micron window gives an actual 1/e spot size of ~14μm. In the vertical direction we move the piezo in small voltage steps and record the detector signal. The result is shown in Figure 4-4. Here, the 1/e width is ~15μm and the actual spot size (after deconvolving) around 12μm. The spot is almost circular and its dimensions are satisfactory for the purpose of this experiment. From now on, we don't touch the input objective and the other aligning mirrors in the setup. Then we place the sample at the objective working distance with the facet as perpendicular as we can see. Looking mainly at the HeNe spot we bring the sample on roughly the right level. Then we use the

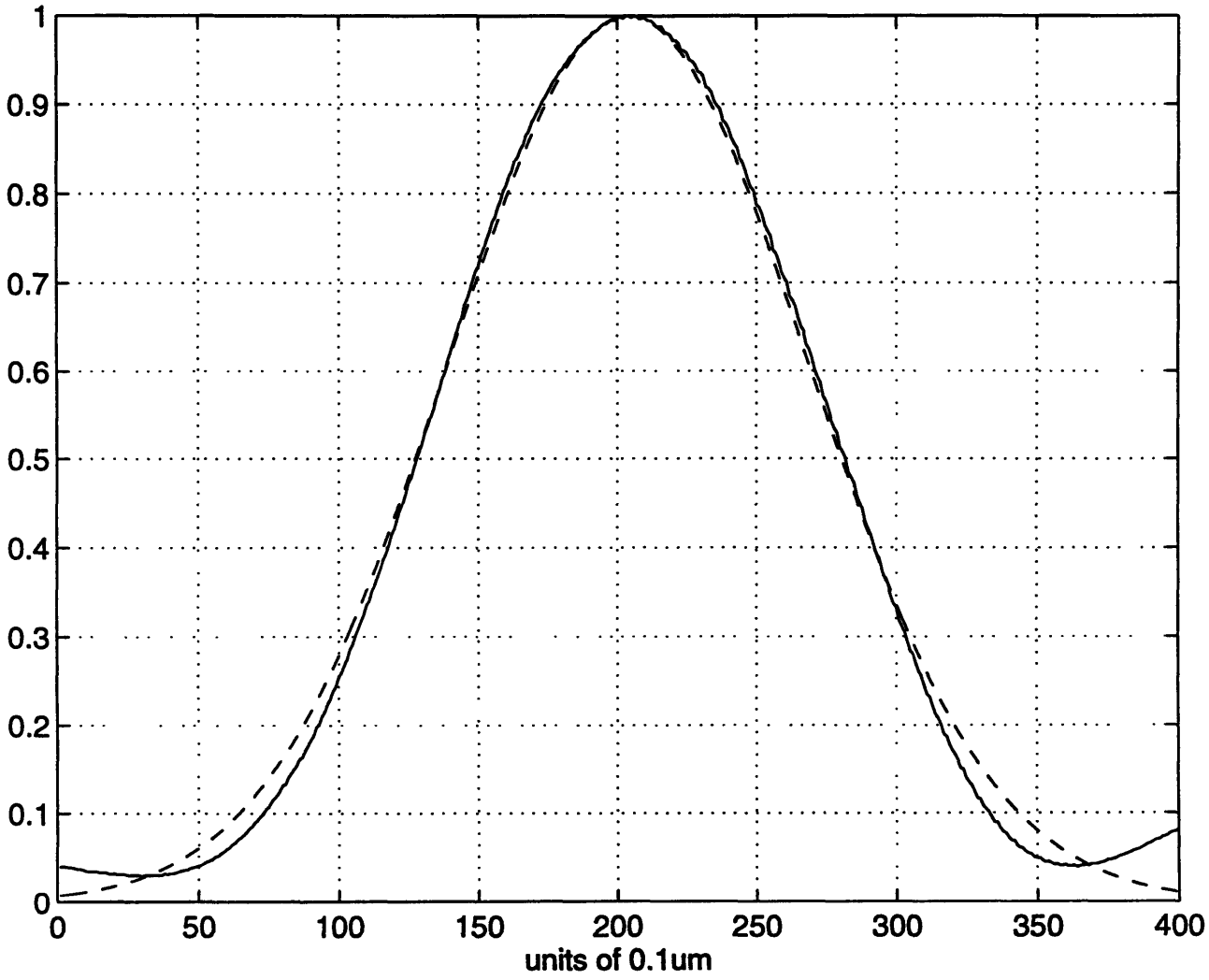

Figure 4-3. Profile of the focused infrared (4.8μm) spot in the horizontal direction. A 18μm Gaussian profile is also shown for comparison.

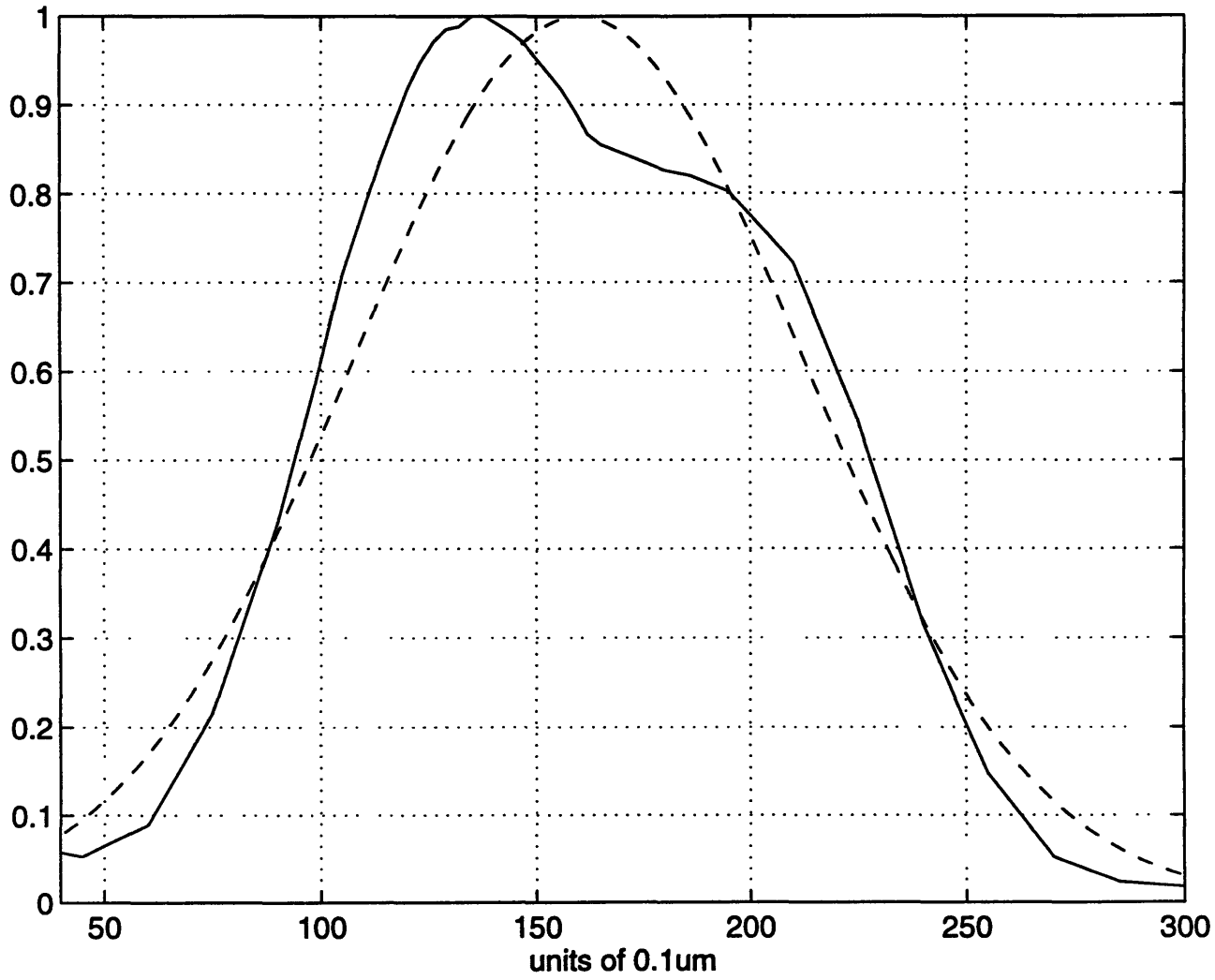

Figure 4-4. Profile of the focused infrared (4.8μm) spot in the vertical direction. A 15μm Gaussian profile is also shown for comparison.

stereoscope and the CCD camera from the top to couple the 980nm light into the structures. When light is coupled the waveguides look bright all the way up to the bridges. Coupling is optimized by moving the sample with the piezotranslators and the goniometer. For the 980nm light we observe that coupling is not extremely sensitive to the angle of incidence and this is because the waveguides are multimode at this wavelength. We also observe that light goes up to the bridges but not through. This happens even with the structures with no holes. The explanation in the case of the structures with holes is that at 980nm light is heavily coupled into the radiation modes of the bridge waveguide (see Figure 1-2) so it is radiated and not transmitted. In the case of the structures with no holes the only explanation that can be given is that the waveguides are still multimode at the waveguide-bridge interface, whereas the structure in the vertical direction as one goes from the guide to the bridge is quite different. We were able to see a very weak spot at the output facet only by looking with a very sensitive ELMO CCD camera and turning up the 980nm diode power to a high level (almost 60mW). This was frustrating because we hoped that the 980 light would go through those structures making the alignment of the setup at the output much easier. The basic problem after the output facet is to distinguish the guided light from the background radiation. The background radiation comes mainly from diffracted light propagating above the structure and is present in a very wide area at the output plane. To deal with this we use the 980 nm light reflected by the glass plate for coupling into the structure from the output facet. To achieve that we use three mirrors to direct light through the collimating objective and couple in the structures from the back side. Now we know the direction that guided light would follow if it was coupled in. An iris is placed at a particular point to select light in this direction only. Although it seems that the background radiation fails to get through the iris a small but nonnegligible portion does and we see that by placing a detector after the closed iris. This could probably suggest that we use a sample not cut at the output facet so that guided light would go at an even larger angle making its separation from the background radiation complete. The next step is to try the infrared light. A good start would be to have some light on the detector right from the beginning and then simply try to optimize it. This is not guaranteed, however, since the waveguides are now single-mode and coupling is sensitive to the angle of incidence (in contrast with the 980nm beam). Up to this point we haven't been successful to couple the IR diode light, possibly because the samples we have so far have not been oxidized in the substrate. Recall from Chapter 2 that the waveguides cannot sustain a mode if the substrate, close to the waveguide-bridge interface, is not

aluminum oxide with the small refractive index of 1.55.

4.3 The Detectors and the Spectrometer

In this paragraph we mention a few things about the detectors and the spectrometer that are used to detect and take spectra of the infrared light. Two infrared detectors are used in this experiment. A room temperature photoconductive PbSe and a nitrogen cooled photovoltaic InSb detector. The PbSe one detects from 1.5 to 5μm and has a maximum D^* of $0.8 \times 10^8 cmHz^{1/2}/W$ at 3.8μm. The minimum detectable power can be calculated from the relation for D^* which is $D^* = SNR\ \Delta f^{1/2}/P\ A^{1/2}$ where SNR is the signal to noise ratio, Δf the lock-in amplifier bandwidth, P the incident power per unit area and A the detector area. Assumming SNR~1, $A=9mm^2$, and Δf=30Hz one finds that the power detection limit is 20nW incident on the entire active area at the peak detectivity wavelength. The InSb detector on the other hand, is a high quality photodiode with excellent performance in the 1 to 5.5μm range. Apart from being nitrogen cooled, it has a very small active area of 250μm diameter and a 60 degree field of view. This results in a background limited performance meaning that the detection limit, as determined by noise, is due to shot noise caused by background radiation instead of thermal noise from the detector itself. Just for comparison, the maximum D^* now is $2 \times 10^{11}\ cmHz^{1/2}/W$ at 5.0μm. The minimum detectable power is found to be around 1pW incident on the detector area. Being extremely sensitive, this detector is going to be used only for the measurement of the bridge spectral response, where the power levels will be very low. For beam finding and alignment and easier detection tasks the less sensitive PbSe detector is going to be used.

The spectrometer used is of the Czerny-Turner configuration employing two large concave mirrors and a plane grating. A collimating mirror collects the radiation from the input slit and spreads the light uniformly over a plane grating. Light diffracted by the grating is collected by a second curved mirror which focuses it back to the exit plane. A variable aperture slit there allows only a very narrow spectral portion of the light to come out and be detected. A spectrum is taken by just rotating the grating and observing the detector signal. The most important parameter in a spectrometer is its wavelength resolution. It is determined by two factors. One is the total number of

grating grooves that are illuminated and the other is the width of the output slit. The first one is given by $\Delta\lambda = \lambda/mN$, where m is the diffracted order from the grating and N is the total number of grooves illuminated. In our case we use a 5cm square grating with a 1.2 μm blaze angle and 150grooves/mm. For the wavelength of 4.5μm this gives a $\Delta\lambda$ of 0.6nm (1st order used) provided that the entire grating area is illuminated. The reason for using a 150gr/mm grating instead of a denser one is that this grating period allows taking spectra up to the 10μm wavelength. We just mention here, that the maximum operating wavelength is roughly given by 2 times the groove spacing, assumming that the first order is used. One can use whichever order he likes to take a spectrum. The difference lies in the fact that lower orders provide larger free spectral range, but smaller resolution. Also, more power goes into the lower orders than into higher ones, although sometimes grating efficiency causes different results. The output slit width determines the spectral bandwidth that is allowed to leave the spectrometer. If this bandwidth is larger than the resolution provided by the grating, then the system performance is limited by the grating. On the other hand, there is no point in reducing the output slit width more than the size determined by the resolution available by the grating. This means reduced throughput at no benefit in resolution. To be more quantitative, the angular dispersion of the grating is given by $m/a \cos\theta$ (in radians per μm) where a is the groove period (in microns) and θ is the angle, with respect to the normal to the grating plane, that the mth order diffracted beam leaves the grating. At the output plane, the units of wavelength per slit-width is given by $\Delta\lambda/\Delta x = a \cos\theta/mL$. L is the grating to the second mirror distance (~ mirror focal length ~ 44cm). For a=1/150, m=1, θ~12 degrees one finds $\Delta\lambda$ ~ 16nm per 1mm slit-width. So if the grating resolution is 1nm, the slit width should be around ~60μm wide. It is really important that one matches, more or less, the spectrometer f number in order to ensure complete filling of the grating with radiation (for maximum resolution) and avoidance of unnecessary losses due to stray light inside the spectrometer. Going at the input slit with a smaller f number, will cause a larger beam than the grating area and reduced throughput in the system. On the other hand focusing at the input with a larger f number, will deteriorate resolution since a smaller area of the objective is illuminated. Losses in spectrometers come primarily from reduced grating efficiency, scattering of light into many orders from which only one is used and the very small output slit width (vignetting loss).

We performed some experiments trying to determine the total losses in the system. We use the lead salt diode emitting at 4.8μm and we collimate the infrared light using a 63mm CaF_2 lens. The

infrared beam diameter is around 8mm. We pass the diode light through two irises and then we use a HeNe beam to go through the irises and in the spectrometer. To focus onto the input slit we use a 63mm focal length CaF_2 lens. For a 8 mm diameter beam this corresponds to a f-number of 7.9. This can be compared to the spectrometer f-number which is 8.8. We align the HeNe beam so that it illuminates the central area of the grating and the two mirrors. We direct one of the orders at the output slit and we image it onto the PbSe detector. A 50mm focal length lens is used to collect the light and focus it back onto the detector. Next, we let the infrared go in and we just rotate the grating to find the first order at the output slit. We narrow the output slit to a 50μm width and redo the imaging at the output. We optimize the alignment by translating the input and output lenses. A program was written for taking spectra, doing averaging and calibrating the spectrometer. The user enters the beginning and final wavelength positions and other parameters as the scanning rate, number of scans and total number of data points taken for the spectrum. Using a source with known spectral emission a spectrum can be taken and then the user can calibrate the instrument moving a cursor on the screen and specifying a wavelength value for a particular feature of the spectrum. The program automatically updates the position of the spectrometer with respect to actual wavelengths. Multiple scans can be run for averaging purposes when the power levels are low. We observed that an improvement in the signal to noise ratio by a factor of ~3 was possible by averaging just 10 scans. Other options of the program include storing and loading spectra into and from files and continuous sampling. The latter enables the user to peak up the detector signal while aligning the system by just looking at the computer screen. Spectra traces were taken by chopping the beam and using a lock-in amplifier to read the detector signal. Changing the diode current we take spectra at various currents using both the PbSe and the cooled InSb detectors. The signal-to-noise ratio is optimized by playing also with the chopping frequency and the lock-in time constant. Increasing the chopping frequency provides better resolution for spectra containing fine features. It also helps sometimes to reduce the lock-in time constant. This means, however, increased noise levels. To increase the signal to noise ratio, we found it very useful sometimes to scan at slower rates. One should be careful of a few things though. First, the chopping frequency cannot and does not need to be too high (above 1.5KHz) because of the bandwidth limitations imposed by the detection circuits. Second, the lock-in time constant has to be sufficiently low for the lock-in to follow the signal changes, but not lower since noise levels are increased. Third, how fast the scanning rate imposes some requirements on the lock-in time constant by itself. In gen-

eral, there are some trade-offs involved and the best way to make sure that everything works properly is to try different things in the lab and see how they work. We were able to take clean spectra of the diode emission even at the threshold current, especially using the InSb detector. One such spectrum is shown in Figure 4-5. It has been taken at the lead-salt diode's threshold (~74mA) and it is centered around 4.81 microns. Only one scan was used and the signal value at the peak is ~150μV. The noise rms value was determined independently to be around 1μV. We measure the power before and after the spectrometer using the PbSe detector (the power levels before are too high for the InSb detector) for various currents. The power after refers to the peak power of the spectrum through the slit. Comparing the measurements we find a power loss factor of ~70 (1.4% transmission). At the diode threshold the power measured before the spectrometer was ~40nW and the signal to noise ratio for the peak value of a spectrum taken with one scan using the InSb detector was 150. This suggests that powers above 250pW before the spectrometer can be measured. One can probably do even better by averaging. We mention here, that the signal to noise ratio when the grating was not moving was around 600 at the peak position. The factor of 70 in losses can be mainly attributed to the grating and the vignetting losses at the output slit. The grating blaze angle is at 1.2μm. From grating efficiency curves this suggests an almost 5-10% transmission at the 4.8μm wavelength. Vignetting losses at the slit are estimated to be around 30%. These together give a transmission of 1.5-3%.

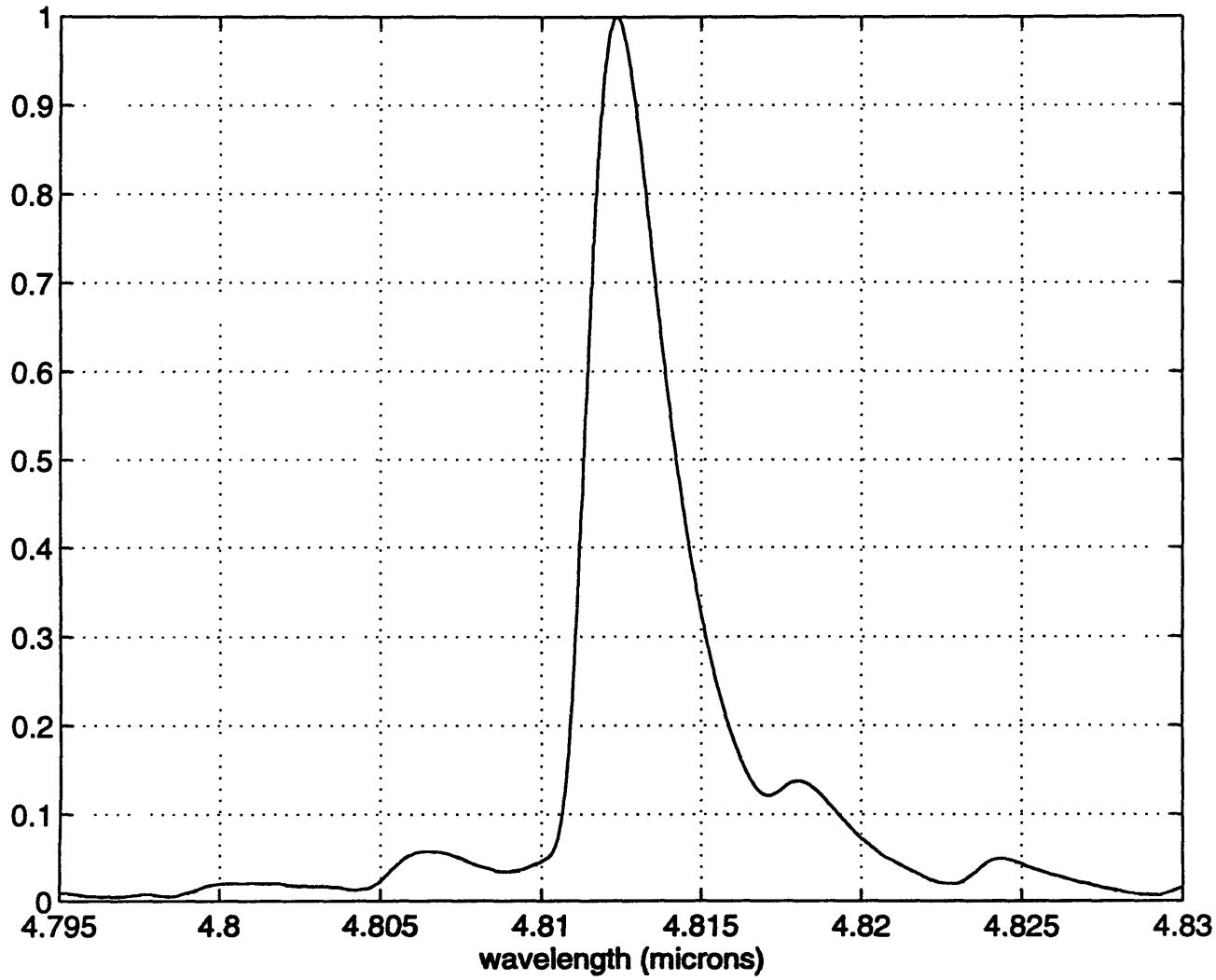

Figure 4-5. Spectrum of the lead-salt diode at the threshold current (one scan).

Chapter 5

Conclusions and Future Work

Photonic bandgap materials can prohibit propagation of light in considerably large frequency ranges. Filters and microlasers with very high quality factors and complete suppression of spontaneous emission and zero-point fluctuations are two promising applications for these materials. Photonic bandgap air-bridge resonators constitute a novel type of filter which uses high-index guiding and a one-dimensional photonic crystal to confine light strongly in all dimensions. A microcavity with modal volume of less than half a cubic wavelength can be realized and the structure is expected to have a very wide bandgap in the near infrared (4-5μm) wavelength range with a resonance centered inside that range. The experimental investigation of such a structure is the goal of this project. To couple light efficiently into and out from the resonators two bent and horizontally tapered waveguides are designed. The experimental setup consists of an Optical Parametric Oscillator (OPO) synchronously pumped by a femtosecond Ti:sapphire laser. The signal and the idler beams produced by the OPO are then combined in a nonlinear crystal to produce femtosecond pulses at the difference frequency. These pulses are tunable at a wide wavelength range from 3 to 5 microns. A coupling stage, featuring some nearly diffraction-limited optics and high precision positioning equipment, follows to couple the light into and out from the structures.

Future work includes generating and coupling femtosecond pulses at the infrared into the air-bridge resonators and taking a spectrum of the light coming at the output. Tuning the wavelength, the full spectral response of the devices can be obtained and compared with the theoretical predic-

tions. Air-Bridge structures at the more attractive, from the optical technology point of view, 1.55 micron wavelength are now being designed for fabrication. The experimental testing of these structures is much easier. Three-dimensional photonic bandgap materials designed for the infrared range of 3 to 5 microns are currently being fabricated at MIT and the same setup developed above for the air-bridges can be used to measure these structures. The trend in the field of photonic bandgap materials is now towards fabricating devices with full two- or three-dimensional photonic bandgaps at the near infrared wavelengths. The main challenge comes from fabrication and developments in that field will determine how fast these exciting, new materials will find their place in optical technology.

References

[1] Yablonovitch, E., (1987) Phys. Rev. Lett. 58, 2059.

[2] John, S., (1987) Phys. Rev. Lett. 58, 2486.

[3] John, S., (1984) Phys. Rev. Lett. 53, 2169.

[4] Anderson, P.W., (1985) Philosophical Magazine B52, 505.

[5] Joannopoulos, J.D., Meade, R.D., Winn, J.N., Photonic Crystals (Princeton, New York, 1995)

[6] John, S., (1996) Photonic Bandgap Materials, NATO ASI Series, Kluwer Academic Publ., ed. by C.M. Soukoulis, 563.

[7] Brown, E.R., Parker, C.D., Yablonovitch, E.J., (1993) J. Opt. Soc. Am. B 10, 404.

[8] Brown, E.R., McMahon, O.B., Parker, C.D., Dill, C., Agi, K., Malloy, K.J., Photonic Bandgap Materials, NATO ASI Series, Kluwer Academic Publ., ed. by C.M. Soukoulis, 355.

[9] Meade, R., Devenyi, A., Joannopoulos, J., Alherhand, O., Smith, D., Kash, K., (1994) J. Appl. Phys. 75, 4753.

[10] Yablonovitch, E., (1993) J. Opt. Soc. Am. B 10, 283.

[11] Ho, K., Chan, C., Soukoulis, C., (1990) Phys. Rev. Lett. 65, 3152.

[12] Yablonovitch, E., Gmitter, T., Leung, K., (1991) Phys. Rev. Lett. 67, 2295.

[13] Photonic Bandgap Materials, NATO ASI Series Vol. 315 (1996), Kluwer Academic Publ., ed. by C.M. Soukoulis.

[14] Fan, S., Villeneuve, P., Meade, R., Joannopoulos, J., (1994) Appl. Phys. Lett. 65, 1446.

[15] Villeneuve, P., Fan, S., Joannopoulos, J., Lim, K.Y., Petrich, G., Kolodziejski, L., Reif, R., (1995) Appl. Phys. Lett. 67, 169.

[16] Chen, J.C., Haus, H.A., Fan, S., Villeneuve, P.R., Joannopoulos, J.D., (1995) J. Lightwave Technol.

[17] Chen, J.C., (1996) Electromagnetic Field Computation and Photonic Bandgap Devices, Ph.D. thesis Massachusetts Institute of Technology.

[18] Spence, D.E., Tang, C.L., (1995) IEEE J. Sel. Top. Quantum Electron. 1, 31.

[19] Kafka, J.D., Watts, M.L., Pieterse, J.W., (1995) J. Opt. Soc. Am. B 12, 2147.

[20] Special feature issue on optical parametric oscillation and amplification, (1993) J. Opt. Soc. Am. B 10, 1655-1791 and 2147-2221.

[21] Special feature issue on optical parametric oscillation and amplification, (1995) J. Opt. Soc. Am. B 12, 2084-2321.

[22] Elsaesser, T., Nuss, M.C., (1991) Opt. Lett. 16, 278.

[23] Ludwig, C., Frey, W., Woerner, M., Elsaesser, T., (1993) Opt. Commun. 102, 447.

[24] Hamm, P., Lauterwasser, C., Zinth, W., (1993) Opt. Lett. 18, 631.

[25] de Barros, M.R.X., Becker, P.C., (1993) Opt. Lett. 18, 631.

[26] de Barros, M.R.X., Miranda, R.S., Jedju, T.M., Becker, P.C., (1994) OSA Tech. Dig. Ser., Vol. 8 (Optical Society of America, Washington DC), post deadline paper BPD 24.

[27] Kafka, J.D., Watts, M.L., Pieterse, J.W., (1994) OSA Tech. Dig. Ser., Vol. 7 (Optical Society of America, Washington DC), 237.

[28] Jedju, T.M., Rothberg, L., (1988) Appl. Opt. 27, 615.

[29] Lohner, A., Kruck, P., Ruhle, W.W., (1994) Appl. Phys. B 59, 211.

[30] Kafka, J.D., Watts, M.L., Pieterse, J.W., Herbst, R.L., (1995) Appl. Phys. B 60, 449.

[31] Wes Wigglesworth, Ealing Electrooptics, personal communication.